AGU PUBLICATIONS

Journal of Advances in Modeling Earth Systems

RESEARCH ARTICLE
10.1002/2016MS000837

Transient aspects of the Hadley circulation forced by an idealized off-equatorial ITCZ

Alex O. Gonzalez[1,2], Gabriela Mora Rojas[3], Wayne H. Schubert[1], and Richard K. Taft[1]

[1]Department of Atmospheric Science, Colorado State University, Fort Collins, Colorado, USA, [2]Now at Joint Institute for Regional Earth System Science and Engineering, University of California, Los Angeles, California, USA, [3]Department of Atmospheric Physics, Oceanography, and Planetary Science, University of Costa Rica, San Pedro Montes de Oca, Costa Rica

Key Points:
- Transient diabatic heating in the ITCZ forces balanced and transient behavior in the southern and northern Hadley cells
- When the ITCZ intensifies within 3 days, equatorially trapped inertia-gravity waves have significantly large amplitudes
- The mass in the Hadley cells oscillate on 1–3 day timescales for typical ITCZ diabatic heating vertical modes

Correspondence to:
A. O. Gonzalez,
alex.o.gonzalez@jpl.nasa.gov

Citation:
Gonzalez, A. O., G. Mora Rojas, W. H. Schubert, and R. K. Taft (2017), Transient aspects of the Hadley circulation forced by an idealized off-equatorial ITCZ, *J. Adv. Model. Earth Syst.*, *9*, 668–690, doi:10.1002/2016MS000837.

Received 15 OCT 2016
Accepted 15 FEB 2017
Accepted article online 20 FEB 2017
Published online 24 MAR 2017

Abstract This paper presents analytical solutions of large-scale, zonally symmetric overturning circulations in the tropical free troposphere forced by transient diabatic heating in the off-equatorial intertropical convergence zone (ITCZ). The dynamics are discussed in the context of the time-dependent meridional circulation equation arising in an equatorial β-plane model. The solutions of these differential equations contain terms for the slow, quasi-balanced part of the response and terms for the transient, zonally symmetric, inertia-gravity wave part of the response. When the off-equatorial (north of the equator) ITCZ diabatic heating is switched on at various rates, both parts of the response reveal a basic asymmetry between the southern and northern hemispheres, with the southern hemisphere side containing most of the quasi-balanced compensating subsidence and transient inertia-gravity wave activity. The inertia-gravity waves travel in wave packets that bounce off a spectrum of turning latitudes and are analyzed in the context of an average conservation law approach. These traveling wave packets cause the mass flux in the southern and northern Hadley cells to pulsate on timescales of about 1, 2, and 3 days for diabatic heating of the external, first internal, and second internal vertical modes, respectively. The spectral characteristics of the vertical motion in the ITCZ and subsidence regions are slightly more complicated and depend on ITCZ location.

1. Introduction

A typical, boreal summer 6.7 μm water vapor image of the eastern Pacific from the GOES West satellite is shown in Figure 1. Under clear-sky conditions, the 6.7 μm channel is sensitive to the vertically averaged humidity in the 200–500 hPa layer, so the dark blue areas on either side of the intertropical convergence zone (ITCZ) indicate regions of low humidity in the upper troposphere and hence regions of enhanced subsidence in the downward branches of the southern hemisphere and northern hemisphere Hadley cells. The complete explanation of atmospheric water vapor distributions can be quite complicated and involve several different physical processes, such as the stretching and folding processes associated with the Rossby wave pattern just east of Hawaii in Figure 1. For detailed discussions of tropical moisture distributions, including trajectory analysis and the concept of "time since last condensation," see *Sun and Lindzen* [1993], *Soden and Fu* [1995], *Salathé and Hartmann* [1997], *Pierrehumbert* [1998], *Pierrehumbert and Roca* [1998], *Galewsky et al*. [2005], *Sherwood et al*. [2006], *Cau et al*. [2007], and *Schreck et al*. [2013]. In spite of the intricacies involved in comprehensive explanations of tropical water vapor distributions, the explanation of the water vapor distribution in the eastern Pacific is simpler than in many other areas during much of the year. An important part of the explanation lies in the large-scale balanced dynamics of the Hadley cells, with the southern hemisphere Hadley cell having larger meridional extent and larger overturning mass flux [*Oort and Rasmusson*, 1970; *Lindzen and Hou*, 1988; *Hack et al*., 1989].

The tropical Hadley circulation is often thought of as a slowly evolving, zonally symmetric phenomenon in which the divergent part of the flow (i.e., the meridional and vertical components) is diagnostically determined via an elliptic equation, while the rotational part of the flow (i.e., the geostrophically balanced zonal component) evolves as the potential vorticity (PV) in the ITCZ develops in response to diabatic and frictional forcing [*Hack et al*., 1989; *Hack and Schubert*, 1990; *Schubert et al*., 1991; *Gonzalez and Mora Rojas*, 2014]. The PV distribution then naturally evolves into a structure in which the meridional gradient of PV has both signs.

© 2017. The Authors.
This is an open access article under the terms of the Creative Commons Attribution-NonCommercial-NoDerivs License, which permits use and distribution in any medium, provided the original work is properly cited, the use is non-commercial and no modifications or adaptations are made.

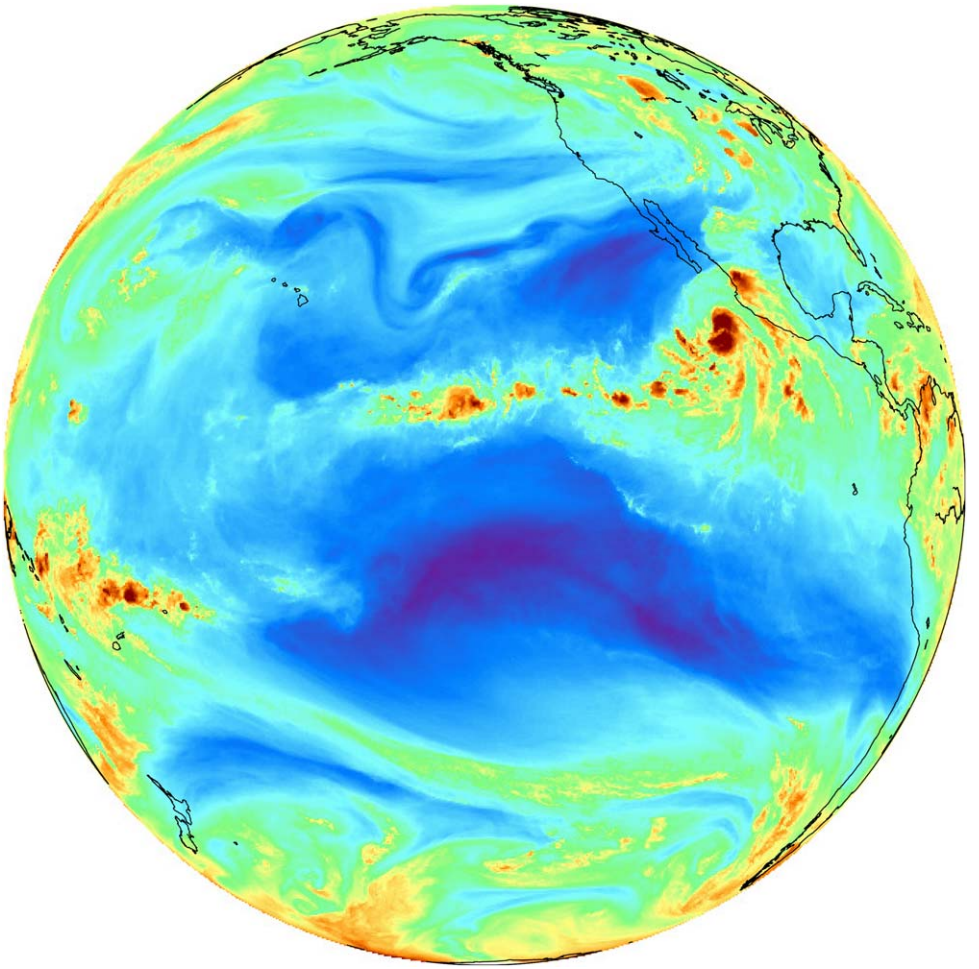

Figure 1. NOAA GOES West satellite water vapor image (6.7 μm) at 06 UTC 25 June 2013. This image is typical of the eastern Pacific during the boreal summer when the ITCZ is located at 10°N–15°N. The dark blue areas on either side of the ITCZ indicate regions of low humidity in the upper troposphere, and hence regions of enhanced subsidence in the downward branches of the southern hemisphere and northern hemisphere Hadley cells.

Such PV structures have the distinct possibility of supporting combined barotropic/baroclinic instability, which leads to a breakdown of the zonally symmetric structure [*Nieto Ferreira and Schubert*, 1997; *Wang and Magnusdottir*, 2005; *Magnusdottir and Wang*, 2008]. In this study, we relax the assumption of geostrophic balance of the zonal flow so that the meridional winds associated with the zonally symmetric Hadley circulation can evolve in a way that allows for the meridional propagation of equatorially trapped inertia-gravity waves. These large-scale inertia-gravity waves are mainly forced by transient convection in the ITCZ.

Inertia-gravity waves in the tropics have been widely studied, but not in the context of the large-scale ITCZ and Hadley circulation system. *Takayabu* [1994] showed evidence that tropospheric inertia-gravity waves, often called "two-day waves," are important for large-scale tropical dynamics, especially in conjunction with the Madden-Julian oscillation. These inertia-gravity waves have been classified as convectively coupled $n = 1$ waves, and they mainly propagate westward, but also have a nonnegligible meridional component [*Haertel and Kiladis*, 2004]. *Wunsch and Gill* [1976] also found observational evidence of $n = 1$ and $n = 2$ inertia-gravity waves in sea level and surface meridional wind data over the central Pacific Ocean, with spectral peaks at 4–5 day timescales. Similar timescales have also been observed in regards to stratospheric inertia-gravity waves forced by tropical convection, as discussed in *Tsuda et al*. [1994], *Karoly et al*. [1996], *Evan and Alexander* [2008], and *Evan et al*. [2012]. In particular, two-day oscillations associated with inertia-gravity waves emanating from tropical convection have been observed in the stratosphere [*Evan and Alexander*, 2008; *Evan et al*., 2012]. The two-day stratospheric inertia-gravity waves travel mainly in the

east-west direction, but do have a meridional component as well [*Evan et al.*, 2012]. It is possible that the tropical free troposphere contains a considerable amount of equatorially trapped inertia-gravity wave activity associated with the ITCZ and Hadley circulation system, but their contribution to the large-scale flow may be difficult to discern in observations and reanalyses.

It is also difficult to correctly initialize inertia-gravity waves because of their small temporal and spatial scales [*Charney*, 1955; *Daley*, 1981]. Therefore, idealized models often filter out inertia-gravity waves [*Gill*, 1980; *Chao*, 1987; *Schubert et al.*, 2009]. Our understanding of transient inertia-gravity waves in the tropics has been limited by a lack of observations, especially over the oceans where the Hadley circulation is strongest. Reanalyses can be used to help our understanding, although they can have problems resolving small-scale inertia-gravity waves sufficiently as they are constrained by their coarse horizontal and vertical resolution. Therefore, idealized modeling of inertia-gravity waves can be useful for improving our understanding of inertia-gravity waves.

In this study, we consider only the flow in the inviscid interior (i.e., above the 900 hPa isobaric surface) following the methods of *Gonzalez and Mora Rojas* [2014]. Our analysis involves solving a partial differential equation in (y, z, t), with appropriate boundary and initial conditions. As described in section 3, the first step to solving this system involves the application of a vertical transform that converts the original partial differential equation in (y, z, t) into a system of partial differential equations in (y, t). *Gonzalez and Mora Rojas* [2014] proceed by using evanescent basis functions, or Green's functions, to solve the slowly forced version of this equation. The Green's function approach yields the most physical insight into the quasi-balanced meridional flow and the fundamental asymmetry between the northern hemisphere and southern hemisphere Hadley cells for an ITCZ centered off of the equator, which is what is typically observed in nature. We use oscillatory basis functions, or the Hermite transform approach, to solve this equation for transient forcings. This approach yields the most physical insight into the transient aspects of the flow and, in particular, how zonally symmetric inertia-gravity waves can be emitted due to transient convection in the ITCZ.

The paper is organized in the following way. In section 2, the primitive equation model is presented and the associated time-dependent meridional circulation equation is derived. A vertical transform is performed in section 3, and section 4 introduces a Hermite transform in y that converts the set of equations in (y, t) into a set of ordinary differential equations in t. In sections 5 and 6, we discuss the free tropospheric response to transient diabatic forcings in the ITCZ with vertical structures comprised solely of one vertical mode. An analysis of inertia-gravity wave packet properties is given in section 7. Some concluding remarks are presented in section 8.

2. Model Equations

In order to gain insight into the transient aspects of the Hadley circulation, we consider zonally symmetric motions in a stratified, compressible atmosphere on the equatorial β-plane. We use $z=H\ \ln(p_0/p)$ as the vertical coordinate, where $p_0=900$ hPa, $T_0=293$ K, $R=287$ J K^{-1} kg^{-1}, and $g=9.81$ m s^{-2} so that $H=RT_0/g \approx 8572$ m. We consider the case of weak horizontal flow and weak baroclinicity, so that the $v(\partial u/\partial y)$ and $w(\partial u/\partial z)$ terms in the zonal momentum equation, the $v(\partial v/\partial y)$ and $w(\partial v/\partial z)$ terms in the meridional momentum equation, and the $v(\partial T/\partial y)$ term in the thermodynamic equation can be neglected. With these simplifications, the governing equations are

$$\frac{\partial u}{\partial t}-\beta y v=0, \tag{1}$$

$$\frac{\partial v}{\partial t}+\beta y u+\frac{\partial \Phi}{\partial y}=0, \tag{2}$$

$$\frac{\partial \Phi}{\partial z}=\frac{g}{T_0}T, \tag{3}$$

$$\frac{\partial v}{\partial y}+\frac{\partial w}{\partial z}-\frac{w}{H}=0, \tag{4}$$

$$\frac{\partial T}{\partial t}+\frac{T_0}{g}N^2 w=\frac{Q}{c_p}, \tag{5}$$

where u is the zonal velocity, v the meridional velocity, w the log-pressure vertical velocity, Φ the perturbation geopotential, T the perturbation temperature, N the constant buoyancy frequency, Q the diabatic heating, and βy the Coriolis parameter.

Our goal is to derive a time-dependent meridional circulation equation. This is a partial differential equation in (y, z, t) that can be solved analytically for a variety of forcings. We begin the derivation by eliminating u between (1) and (2), yielding

$$\frac{\partial}{\partial y}\left(\frac{\partial \Phi}{\partial t}\right)+\left(\frac{\partial^2}{\partial t^2}+\beta^2 y^2\right)v=0. \tag{6}$$

Similarly, from the elimination of T between (3) and (5) we obtain

$$\frac{\partial}{\partial z}\left(\frac{\partial \Phi}{\partial t}\right)+N^2 w=\frac{gQ}{c_p T_0}. \tag{7}$$

The elimination of $(\partial\Phi/\partial t)$ between (6) and (7) then yields

$$N^2\frac{\partial w}{\partial y}-\left(\frac{\partial^2}{\partial t^2}+\beta^2 y^2\right)\frac{\partial v}{\partial z}=\frac{g}{c_p T_0}\frac{\partial Q}{\partial y}. \tag{8}$$

Equations (4) and (8) can be regarded as a closed system in v and w. One way of proceeding from this system is to make use of (4) to express the meridional circulation components $v(y,z,t)$ and $w(y,z,t)$ in terms of the stream function $\psi(y,z,t)$ by

$$e^{-z/H}v=-\frac{\partial \psi}{\partial z} \quad \text{and} \quad e^{-z/H}w=\frac{\partial \psi}{\partial y}, \tag{9}$$

and then to use (9) in (8) to obtain a single equation in ψ. This procedure yields the time-dependent meridional circulation equation that is given below in (10). Assuming that $v \to 0$ as $y \to \pm\infty$ and that w vanishes at the top boundary ($z=z_T$), we obtain the boundary conditions given below in (12) and (13). Following *Gonzalez and Mora Rojas* [2014], we assume that the actual vertical velocity (i.e., the physical height vertical velocity) is specified at the lower isobaric surface $z=0$ (i.e., the top of the boundary layer) for the lower boundary condition. Concerning the initial conditions, we assume that the meridional circulation and its tendency both vanish at $t=0$.

In summary, the time-dependent meridional circulation equation is

$$\left(\frac{\partial^2}{\partial t^2}+\beta^2 y^2\right)\left(\frac{\partial^2 \hat{\psi}}{\partial z^2}-\frac{\hat{\psi}}{4H^2}\right)+N^2\frac{\partial^2 \hat{\psi}}{\partial y^2}=\frac{g}{c_p T_0}\frac{\partial \hat{Q}}{\partial y}, \tag{10}$$

where

$$\begin{aligned}\hat{\psi}(y,z,t) &= \psi(y,z,t)\,e^{z/2H},\\ \hat{Q}(y,z,t) &= Q(y,z,t)\,e^{-z/2H},\end{aligned} \tag{11}$$

with boundary conditions

$$\hat{\psi} \to 0 \quad \text{as} \quad y \to \pm\infty, \tag{12}$$

$$\hat{\psi}=0 \quad \text{at} \quad z=z_T, \tag{13}$$

$$\left(\frac{\partial^2}{\partial t^2}+\beta^2 y^2\right)\left(\frac{\partial \hat{\psi}}{\partial z}-\frac{\hat{\psi}}{2H}\right)+g\frac{\partial^2 \hat{\psi}}{\partial y^2}=g\frac{\partial \mathcal{W}}{\partial y} \quad \text{at} \quad z=0, \tag{14}$$

where $\mathcal{W}(y,t)$ is the physical height vertical velocity at $z=0$, and with initial conditions

$$\hat{\psi}=0 \quad \text{and} \quad \frac{\partial \hat{\psi}}{\partial t}=0 \quad \text{at} \quad t=0. \tag{15}$$

The use of (11) simplifies the time-dependent meridional circulation equation (10) by eliminating the $e^{z/H}$ factors. Note that the diabatic forcing appears through the right-hand side of the interior equation (10) while the frictional forcing appears through the right-hand side of the lower boundary condition (14).

The first step in solving the time-dependent meridional circulation problem (10)–(15) involves a vertical transform of (10), which is presented in section 3. This vertical transform converts (10) from a partial differential equation in (y, z, t) to a system of partial differential equations in (y, t), as shown in (28). There are two

methods that can be used to proceed from (28). The first method involves using a Green's function approach that has evanescent basis functions; this was explored in *Gonzalez and Mora Rojas* [2014]. The second method involves a Hermite transform that contains oscillatory basis functions as is presented in section 4.

3. Vertical Transform of the Meridional Circulation Equation

We seek solutions of (10)–(15) via the vertical transform pair [*Fulton and Schubert*, 1985; *Gonzalez and Mora Rojas*, 2014]

$$\hat{\psi}(y,z,t)=\sum_{m=0}^{\infty}\hat{\psi}_m(y,t)\,\mathfrak{Z}_m(z), \tag{16}$$

$$\hat{\psi}_m(y,t)=\frac{N^2}{g}\int_0^{z_T}\hat{\psi}(y,z,t)\,\mathfrak{Z}_m(z)\,dz+\hat{\psi}(y,0,t)\,\mathfrak{Z}_m(0). \tag{17}$$

In other words, the stream function $\hat{\psi}(y,z,t)$ is represented in terms of a series of vertical structure functions $\mathfrak{Z}_m(z)$, with the coefficients $\hat{\psi}_m(y,t)$ given by equation (17). The last term in (17) may seem unfamiliar; it arises from the lower boundary condition (14). The vertical structure functions $\mathfrak{Z}_m(z)$ are solutions of the Sturm-Liouville eigenvalue problem

$$\frac{d^2\mathfrak{Z}_m}{dz^2}-\frac{\mathfrak{Z}_m}{4H^2}=-\frac{N^2\mathfrak{Z}_m}{gh_m}, \tag{18}$$

$$\mathfrak{Z}_m=0 \quad \text{at} \quad z=z_T, \tag{19}$$

$$\frac{d\mathfrak{Z}_m}{dz}-\frac{\mathfrak{Z}_m}{2H}=-\frac{\mathfrak{Z}_m}{h_m} \quad \text{at} \quad z=0, \tag{20}$$

with eigenvalues (or equivalent depths) denoted by h_m. Since the eigenvalue h_m appears in both the differential equation (18) and the lower boundary condition (20), this Sturm-Liouville problem is slightly more general than those usually treated in standard texts. A discussion of the transform pair (16) and (17) is given in *Gonzalez and Mora Rojas* [2014, Appendices], along with a proof that $h_m > 0$, a derivation of the solutions $\mathfrak{Z}_m(z)$, as well as an analysis of the completeness of the set $\mathfrak{Z}_m(z)$ for $m=0,1,2,\cdots$, and a discussion of the associated orthonormality relation.

Defining $\hat{h}=(2NH)^2/g\approx 4314$ m, corresponding to our choice $N=1.2\times10^{-2}$ s^{-1}, we can organize the solutions of equations (18–20) into two cases: $h_m>\hat{h}$ (Case 1), which results in evanescent behavior of the eigenfunction; and $0<h_m<\hat{h}$ (Case 2), which results in oscillatory behavior of the eigenfunction. For Case 1 there is only one eigenvalue, denoted by the external mode h_0. For Case 2 there is an infinite set of eigenvalues, denoted by the internal modes $h_1,h_2,\cdots$. In summary, the corresponding eigenfunctions are

$$\mathfrak{Z}_m(z)=\begin{cases}A_0\sinh\left[\kappa_0(1-z/z_T)\right] & \text{if} \quad m=0,\\ A_m\sin\left[\kappa_m(1-z/z_T)\right] & \text{if} \quad m\geq 1,\end{cases} \tag{21}$$

where κ_0 and κ_m ($m\geq 1$) are related to the eigenvalues h_m through the formula given below as equation (26). The normalization factor for the external mode $m=0$ is

$$A_0=\left\{\frac{N^2z_T}{2g}\left[\frac{\sinh(\kappa_0)\cosh(\kappa_0)}{\kappa_0}-1\right]+\sinh^2(\kappa_0)\right\}^{-\frac{1}{2}}, \tag{22}$$

and the normalization factors for the internal modes $m\geq 1$ are

$$A_m=\left\{\frac{N^2z_T}{2g}\left[1-\frac{\sin(\kappa_m)\cos(\kappa_m)}{\kappa_m}\right]+\sin^2(\kappa_m)\right\}^{-\frac{1}{2}}. \tag{23}$$

As can be shown by substituting $z=z_T$ into (21), the eigenfunctions satisfy the upper boundary condition (19). Through application of the lower boundary condition (20), it can be shown that κ_0 is the solution of the transcendental equation

Table 1. Information About the First Five Vertical Modes[a]

m	h_m (m)	c_m (m s^{-1})	$\bar{b}_m$ (km)
0	7095	263.8	3394
1	229.5	47.45	1440
2	61.36	24.53	1035
3	27.63	16.46	848.1
4	15.61	12.38	735.2

[a]The spectra of equivalent depths h_m, gravity wave speeds $c_m=(gh_m)^{1/2}$, and equatorial Rossby lengths $\bar{b}_m=(c_m/\beta)^{1/2}$ for the five values of m listed in the left column, where the values have been computed from (26) using $z_T=13$ km, $N=1.2\times10^{-2}$ s^{-1}, and $H=8572$ m.

$$\tanh(\kappa_0)=\frac{\kappa_0}{(z_T/\hat{h})[1-\hat{h}/(2H)-(2H\kappa_0/z_T)^2]}, \tag{24}$$

while the κ_m are the solutions of the transcendental equation

$$\tan(\kappa_m)=\frac{\kappa_m}{(z_T/\hat{h})[1-\hat{h}/(2H)+(2H\kappa_m/z_T)^2]}. \tag{25}$$

After the transcendental equations (24) and (25) are solved, the equivalent depths h_m can be obtained from

$$h_m=\begin{cases}\hat{h}\left[1-(2H\kappa_0/z_T)^2\right]^{-1} & \text{if} \quad m=0,\\ \hat{h}\left[1+(2H\kappa_m/z_T)^2\right]^{-1} & \text{if} \quad m\geq 1.\end{cases} \tag{26}$$

The first five eigenvalues h_m (m=0, 1, 2, 3, 4) are listed in the second column of Table 1, while the corresponding eigenfunctions $\mathcal{Z}_m(z)$ are shown in *Gonzalez and Mora Rojas* [2014, Figure 2]. Note that the dependence of the normalization factors A_m on m is weak because $\kappa_m\approx m\pi$, making the sin(κ_m) terms in equation (23) negligible, leading to $A_m\approx[2g/(N^2z_T)]^{1/2}\approx 3.2$. The solution of equation (24) is $\kappa_0\approx 0.4747$.

To take the vertical transform of equation (10), we first multiply it by $\mathcal{Z}_m(z)$ and integrate over z from 0 to z_T. The integral involving the second-order vertical derivative term in (10) is then integrated by parts twice, yielding

$$\begin{aligned}&\left(\frac{\partial^2}{\partial t^2}+\beta^2y^2\right)\left[\mathcal{Z}_m\left(\frac{\partial\hat{\psi}}{\partial z}-\frac{\hat{\psi}}{2H}\right)-\hat{\psi}\left(\frac{d\mathcal{Z}_m}{dz}-\frac{\mathcal{Z}_m}{2H}\right)\right]_0^{z_T}\\ &+\left(\frac{\partial^2}{\partial t^2}+\beta^2y^2\right)\int_0^{z_T}\hat{\psi}\left(\frac{d^2\mathcal{Z}_m}{dz^2}-\frac{\mathcal{Z}_m}{4H^2}\right)dz\\ &+N^2\frac{\partial^2}{\partial y^2}\int_0^{z_T}\hat{\psi}\mathcal{Z}_m\,dz=\frac{g}{c_pT_0}\frac{\partial}{\partial y}\int_0^{z_T}\hat{Q}\mathcal{Z}_m\,dz.\end{aligned} \tag{27}$$

To simplify (27), first use (18) in the second line and then use (13) and (19) to show that the upper boundary term in the first line vanishes. To evaluate the lower boundary term in the first line, we use (14) to eliminate $[(\partial\hat{\psi}/\partial z)-(\hat{\psi}/2H)]$ and then group the resulting terms with the third line of (27). Similarly, we use (20) to eliminate $[(d\mathcal{Z}_m/dz)-(\mathcal{Z}_m/2H)]$ and then group the resulting $\mathcal{Z}_m/h_m$ term with the second line of (27). Making use of (17), this procedure then simplifies (27) to

$$\frac{\partial^2\hat{\psi}_m}{\partial t^2}-gh_m\left(\frac{\partial^2}{\partial y^2}-\frac{y^2}{\bar{b}_m^4}\right)\hat{\psi}_m=-gh_m\frac{\partial F_m}{\partial y}, \tag{28}$$

with boundary conditions

$$\hat{\psi}_m\to 0 \text{ as } y\to\pm\infty, \tag{29}$$

and with initial conditions

$$\hat{\psi}_m=0 \quad \text{and} \quad \frac{\partial\hat{\psi}_m}{\partial t}=0 \quad \text{at} \quad t=0, \tag{30}$$

where the equatorial Rossby length is defined by $\bar{b}_m=(c_m/\beta)^{1/2}$. The forcing term $F_m(y,t)$ on the right-hand side of (28) is given by

$$F_m(y,t)=\frac{g\hat{Q}_m(y,t)}{c_pT_0N^2}+\left(\mathcal{W}(y,t)-\frac{g\hat{Q}(y,0,t)}{c_pT_0N^2}\right)\mathcal{Z}_m(0), \tag{31}$$

where

$$\hat{Q}_m(y,t)=\frac{N^2}{g}\int_0^{z_T}\hat{Q}(y,z,t)\mathcal{Z}_m(z)\,dz+\hat{Q}(y,0,t)\mathcal{Z}_m(0). \tag{32}$$

Note that the $\bar{b}_m$ definition of Rossby length is convenient when working with Hermite functions $\mathcal{H}_n^m(y)$ that we use in the next section, while the $b_m=\bar{b}_m/\sqrt{2}$ definition of equatorial Rossby length is convenient when working with parabolic cylinder functions $D_n(y)$ [*Gonzalez and Mora Rojas*, 2014].

4. Solution via Hermite Transforms

The solution of (28)–(32) is now constructed by using Hermite transform methods. The Hermite transform pair for the stream function is

$$\hat{\psi}_m(y,t)=\sum_{n=0}^{\infty}\hat{\psi}_{mn}(t)\,\mathcal{H}_n^m(y), \tag{33}$$

$$\hat{\psi}_{mn}(t)=\frac{1}{\bar{b}_m}\int_{-\infty}^{\infty}\hat{\psi}_m(y,t)\,\mathcal{H}_n^m(y)\,dy, \tag{34}$$

where the meridional structure functions $\mathcal{H}_n^m(y)$ are related to the Hermite polynomials $H_n(y/\bar{b}_m)$ by

$$\mathcal{H}_n^m(y)=\left(\pi^{\frac{1}{2}}2^n n!\right)^{-\frac{1}{2}}H_n(y/\bar{b}_m)\,e^{-\frac{1}{2}(y/\bar{b}_m)^2}. \tag{35}$$

Since the Hermite polynomials satisfy the recurrence relation $H_{n+1}(x)=2xH_n(x)-2nH_{n-1}(x)$, it can be shown that the meridional structure functions $\mathcal{H}_n^m(y)$ satisfy the recurrence relation

$$\mathcal{H}_{n+1}^m(y)=\left(\frac{2}{n+1}\right)^{\frac{1}{2}}\left(\frac{y}{\bar{b}_m}\right)\mathcal{H}_n^m(y)-\left(\frac{n}{n+1}\right)^{\frac{1}{2}}\mathcal{H}_{n-1}^m(y). \tag{36}$$

We first compute $\mathcal{H}_0^m(y)$ from $H_0(x)=1$, obtaining $\mathcal{H}_0^m(y)=\pi^{-\frac{1}{4}}e^{-\frac{1}{2}(y/\bar{b}_m)^2}$. All succeeding Hermite functions can be computed using the recurrence relation (36), with the understanding that the last term in (36) vanishes when $n=0$. Computing $\mathcal{H}_n^m$ via its recurrence relation is much preferable to computing H_n via its recurrence relation and then computing $\mathcal{H}_n^m$ by evaluation of the right-hand side of (35), because the former method avoids explicit calculation of the factor $2^n n!$ for large n. Plots of $\mathcal{H}_n^m(y)$ for $m=0$, 1, 2 and $n=0$, 1, 2, 3, 4 are shown in the three panels of Figure 2.

The meridional structure functions satisfy the second-order equation

$$\left(\frac{d^2}{dy^2}-\frac{y^2}{\bar{b}_m^4}\right)\mathcal{H}_n^m(y)=-\left(\frac{2n+1}{\bar{b}_m^2}\right)\mathcal{H}_n^m(y), \tag{37}$$

so that $\mathcal{H}_n^m(y)$ is an eigenfunction of the operator that appears in parentheses on the left-hand side of (28). This eigenfunction property makes the transform pair (33) and (34) convenient for the solution of (28). Note that solutions of (37) transition from oscillatory to evanescent when $\tilde{y}_{mn}=\pm\bar{b}_m\,(2n+1)^{1/2}$, which we define as the turning (or critical) latitudes [*Wunsch and Gill*, 1976]. In Table 2, we display the turning latitudes for vertical modes $m=0,1,2,3,4$ and meridional modes $n=0,1,2,3,4$.

Another convenient property of the meridional structure functions $\mathcal{H}_n^m(y)$ is that they satisfy the orthonormality relation

$$\int_{-\infty}^{\infty}\mathcal{H}_n^m(y)\,\mathcal{H}_{n'}^m(y)\,dy=\begin{cases}\bar{b}_m & n'=n,\\ 0 & n'\neq n.\end{cases} \tag{38}$$

Note that (34) can be obtained through multiplication of (33) by $\mathcal{H}_{n'}^m(y)$, followed by integration over y and use of (38).

To take the meridional transform of (28), first multiply it by $\mathcal{H}_n^m(y)$ and integrate over y. The integral involving the second-order y-derivative term in (28) is then integrated by parts twice, making use of the boundary conditions (30), to yield

$$\begin{aligned}\frac{\partial^2}{\partial t^2}\int_{-\infty}^{\infty}\hat{\psi}_m(y,t)\mathcal{H}_n^m(y)\,dy-gh_m\int_{-\infty}^{\infty}\hat{\psi}_m(y,t)\left(\frac{d^2}{dy^2}-\frac{y^2}{\bar{b}_m^4}\right)\mathcal{H}_n^m(y)\,dy\\ =-gh_m\int_{-\infty}^{\infty}\frac{\partial F_m(y,t)}{\partial y}\mathcal{H}_n^m(y)\,dy.\end{aligned} \tag{39}$$

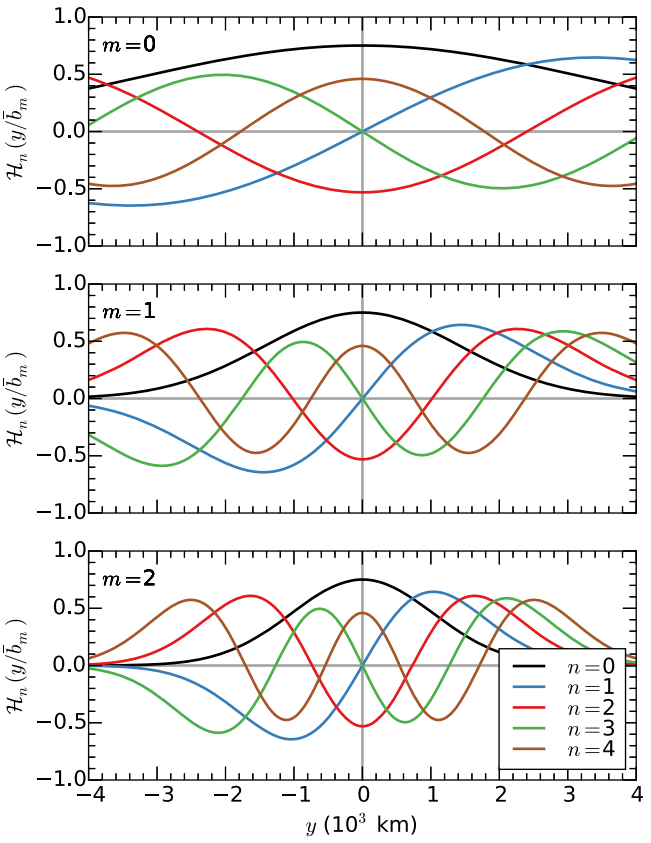

Figure 2. Plots of $\mathcal{H}_n^m(y)$ for $m = 0, 1, 2$ and $n = 0, 1, 2, 3, 4$. Note that, as n increases (for a given m), the width of the oscillatory region of $\mathcal{H}_n^m(y)$ increases as $n^{1/2}$, so the magnitude of $\mathcal{H}_n^m(y)$ in the oscillatory region decreases as $n^{-1/4}$ in order to satisfy the normalization imposed by (38).

To simplify (39) we first use (37) in the integrand of the second integral. We then make use of (34) to simplify (39) to the second-order ordinary differential equation

$$\frac{d^2\hat{\psi}_{mn}}{dt^2} + \nu_{mn}^2\hat{\psi}_{mn} = -gh_m F'_{mn}, \tag{40}$$

with the initial conditions

$$\hat{\psi}_{mn} = 0 \text{ and } \frac{d\hat{\psi}_{mn}}{dt} = 0 \text{ at } t = 0, \tag{41}$$

where the inertia-gravity wave frequency ν_{mn} is given by

$$\nu_{mn} = \frac{1}{\bar{b}_m}[gh_m(2n+1)]^{1/2}, \tag{42}$$

and the forcing by

$$F'_{mn}(t) = \frac{1}{\bar{b}_m}\int_{-\infty}^{\infty}\frac{\partial F_m(y,t)}{\partial y}\mathcal{H}_n^m(y)\,dy. \tag{43}$$

The inertia-gravity wave frequencies for the first five vertical wave numbers ($m = 0, 1, 2, 3, 4$) are shown as a function of meridional mode n in Figure 3. Values of the γ^{-1} parameter in the switch-on function $\mathcal{T}(t)$, presented in the next section, are plotted in the four horizontal dashed lines, $\gamma^{-1} = 3,\ 6,\ 12,\ 24$ h. Notice how $\gamma^{-1} = 24$ h does not intersect with any of the $m = 0, 1, 2, 3, 4$ inertia-gravity wave frequencies. As will be seen later, when diabatic heating is switched on at this slow rate, inertia-gravity wave activity is minimal and the transient solutions are approximately equal to the balanced solutions derived in *Gonzalez and Mora Rojas* [2014]. In the next section, we solve (40) and (41) for a particular forcing.

5. Transient Hadley Circulations Forced by a Switch-On of ITCZ Convection

Consider the response to a forcing for which the Ekman pumping and the diabatic heating at $z = 0$ are related by

$$\mathcal{W}(y,t) = \frac{g\hat{Q}(y,0,t)}{c_p T_0 N^2}, \tag{44}$$

so that (31) simplifies to

$$F_m(y,t) = \frac{g\hat{Q}_m(y,t)}{c_p T_0 N^2}. \tag{45}$$

This relation between the Ekman pumping and diabatic heating is assumed in order to use the vertical structure of a single vertical mode to represent the vertical structure of the prescribed diabatic heating. For example, the vertical structure of $\mathfrak{Z}_1(z)$ is not equal to zero at $z = 0$ therefore there must be a small nonzero vertical velocity at $z = 0$. This simplification can be avoided if the prescribed diabatic heating were equal

Table 2. Information About the Turning Latitudes[a]

m	$n=0$	$n=1$	$n=2$	$n=3$	$n=4$
0	3,395	5,880	7,590	8,981	10,184
1	1,440	2,494	3,230	3,809	4,319
2	1,035	1,793	2,315	2,739	3,106
3	848.1	1,469	1,896	2,244	2,544
4	735.3	1,274	1,644	1,945	2,206

[a]The turning latitudes in the units of km for $m=0, 1, 2, 3, 4$ and $n=0, 1, 2, 3, 4$ using the formula $\tilde{y}_{mn}=\pm\bar{b}_m(2n+1)^{1/2}$. Note how the turning latitudes increase as the meridional mode n increases and the vertical mode m decreases.

zero at $z=0$. However, more than one vertical heating mode would be required to represent this behavior. For brevity, we proceed using only single vertical modes.

Assume that $\hat{Q}(y,z,t)$ vanishes everywhere except in the latitudinal range $y_1<y<y_2$, where y_1 and y_2 are constants that specify the south and north boundaries of the ITCZ. Within this ITCZ region, the diabatic heating is assumed to be independent of y and to be smoothly switched on to a steady state value, i.e.,

$$\hat{Q}(y,z,t)=\mathcal{T}(t)\begin{cases}\sum_{m=0}^{\infty}\tilde{Q}_m\mathcal{Z}_m(z) & \text{if } y_1<y<y_2,\\ 0 & \text{otherwise,}\end{cases} \tag{46}$$

where the constants $\tilde{Q}_m$ specify the projection of the vertical structure of $\hat{Q}(y,z,t)$ onto the vertical modes, and where the time dependence is given by

$$\mathcal{T}(t)=1-(1+\gamma t)e^{-\gamma t}, \tag{47}$$

with the constant γ specifying the sharpness of the switch-on function $\mathcal{T}(t)$. Figure 4 displays four $\mathcal{T}(t)$ curves for the particular values $\gamma^{-1}=3, 6, 12, 24$ h.

Substituting (46) into (32), and then using the orthonormality relation associated with $\mathcal{Z}_m(z)$, we obtain

$$\hat{Q}_m(y,t)=\mathcal{T}(t)\begin{cases}\tilde{Q}_m & \text{if } y_1<y<y_2,\\ 0 & \text{otherwise.}\end{cases} \tag{48}$$

Use of (45) and (47) in (43) now yields

$$F'_{mn}(t)=\frac{g\mathcal{H}_n^m(y_1)}{c_pT_0N^2\bar{b}_m}\int_{y_1-}^{y_1+}\frac{\partial\hat{Q}_m(y,t)}{\partial y}dy+\frac{g\mathcal{H}_n^m(y_2)}{c_pT_0N^2\bar{b}_m}\int_{y_2-}^{y_2+}\frac{\partial\hat{Q}_m(y,t)}{\partial y}dy=\mathcal{T}(t)\mathcal{F}_{mn}, \tag{49}$$

where

$$\mathcal{F}_{mn}=\frac{g\tilde{Q}_m}{c_pT_0N^2\bar{b}_m}\left[\mathcal{H}_n^m(y_1)-\mathcal{H}_n^m(y_2)\right], \tag{50}$$

and where we have made use of the fact that the narrow integral of $(\partial\hat{Q}_m/\partial y)$ across y_1 is $\tilde{Q}_m\mathcal{T}(t)$ and the narrow integral across y_2 is $-\tilde{Q}_m\mathcal{T}(t)$.

The final equality in (49) can now be used in the right-hand side of (40), and the complete solution can be written as the sum of the homogeneous solution and a particular solution. As can be checked by direct substitution into (40), the solution satisfying the initial conditions (41) is

$$\hat{\psi}_{mn}(t)=\Psi_{mn}\left\{\left(\frac{(\nu_{mn}^2-\gamma^2)\gamma^2}{(\nu_{mn}^2+\gamma^2)^2}\right)\cos(\nu_{mn}t)-\left(\frac{2\gamma^3\nu_{mn}}{(\nu_{mn}^2+\gamma^2)^2}\right)\sin(\nu_{mn}t)\right.$$
$$\left.+1-\left(\frac{\nu_{mn}^2+3\gamma^2}{\nu_{mn}^2+\gamma^2}+\gamma t\right)\left(\frac{\nu_{mn}^2e^{-\gamma t}}{\nu_{mn}^2+\gamma^2}\right)\right\}, \tag{51}$$

where $\Psi_{mn}=-gh_m\mathcal{F}_{mn}/\nu_{mn}^2$. In summary, the solution of the original meridional circulation problem is obtained by combining equations (11), (16), and (33), yielding

$$\psi(y,z,t)=e^{-z/2H}\sum_{m=0}^{\infty}\sum_{n=0}^{\infty}\hat{\psi}_{mn}(t)\,\mathcal{H}_n^m(y)\,\mathcal{Z}_m(z), \tag{52}$$

where $\hat{\psi}_{mn}(t)$ is given by equation (51). Plots of the stream function can be constructed by first calculating $\mathcal{F}_{mn}$ from (50), then calculating $\hat{\psi}_{mn}(t)$ from (51), and finally calculating $\psi(y,z,t)$ from (52).

Note that when $\gamma\ll\nu_{mn}$, the solution (51) simplifies considerably since the coefficients of the $\cos(\nu_{mn}t)$ and $\sin(\nu_{mn}t)$ terms become much smaller than unity, while the second line in (51) approaches $\mathcal{T}(t)$. Then, the spectral space solution (51) simplifies to

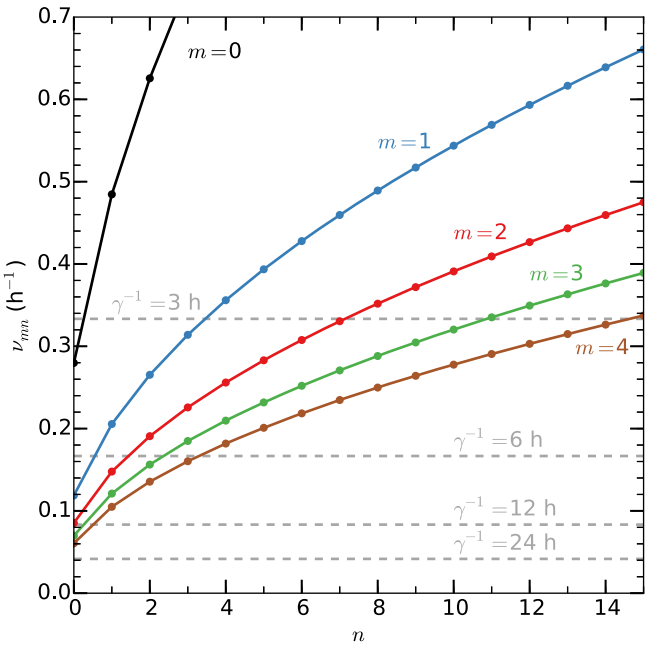

Figure 3. Plots of ν_{mn}, computed from (42), for $m=0, 1, 2, 3$, and 4 and $n=0, 1, \ldots, 15$. The four horizontal dashed lines indicate the values of γ corresponding to the four switch-on functions $\mathcal{T}(t)$ presented in (47) and plotted in Figure 4.

$$\hat{\psi}^{(b)}_{mn}(t)=\Psi_{mn}\mathcal{T}(t) \tag{53}$$

so that the physical space solution (52) becomes

$$\psi^{(b)}(y,z,t)=e^{-z/2H}\sum_{m=0}^{\infty}\sum_{n=0}^{\infty}\hat{\psi}^{(b)}_{mn}(t)\,\mathcal{H}^{m}_{n}(y)\,\mathfrak{Z}_{m}(z), \tag{54}$$

where the superscript (b) indicates the balanced (or filtered) solution. Since the time dependence on the right-hand side of (53) is $\mathcal{T}(t)$, the $\psi^{(b)}(y,z,t)$ field develops in lock-step with the forcing, i.e., there is no time delay between the forcing and the response, no matter how far one is from the forcing. Since this represents "action at a distance," it should be regarded as a filtered approximation of the actual dynamics, valid only in the case of a "slowly varying forcing." To better understand how slow the forcing needs to be, Figure 3 includes horizontal dashed lines for the four values of γ used in Figure 4. As an example, for $m=1$ and $\gamma^{-1}=24$ h the condition $\gamma \ll \nu_{mn}$ holds for essentially all n, while for $m=1$ and $\gamma^{-1}=3$ h the condition does not hold for the smaller values of n. Thus, for the external mode and the first two internal modes, the $\gamma^{-1}=24$ h dashed line in Figure 3 would correspond to a forcing that is probably slow enough for the filtered approximation to be reasonably accurate, but the $\gamma^{-1}=3$ h dashed line would correspond to a forcing that excites a nonnegligible inertia-gravity wave response, especially for the higher internal modes. This hypothesis will be confirmed by the examples shown in the next section.

6. Examples Using Single Vertical Mode Diabatic Heating

6.1. Diabatic Heating of the $m=1$ Mode

In this section, we present examples forced by diabatic heating in an ITCZ centered off of the equator with a simplified single vertical mode structure. We begin with a diabatic heating of the first internal mode $m=1$, given by

$$\frac{\tilde{Q}_m}{c_p}=\begin{cases}(5\,\mathrm{K\ d^{-1}})\left(\dfrac{500\,\mathrm{km}}{y_2-y_1}\right) & \text{if } m=1,\\ 0 & \text{if } m\neq 1,\end{cases} \tag{55}$$

where $\tilde{Q}_m$ has been normalized in such a way that the horizontally integrated forcing $(y_2-y_1)\tilde{Q}_m$ is fixed.

Figures 5 and 6 show isolines of $\psi(y,z,t)$ and contour shading of $Q(y,z,t)e^{-z/H}/c_p$ at $t=12$, 36, 60, 84 h and $t=108$, 132, 156, 180 h for the switch on rates $\gamma^{-1}=3$ h and $\gamma^{-1}=24$ h, respectively. The ψ field is computed from (52) using the parameter choices $z_T=13$ km, $N=1.2\times10^{-2}$ s^{-1}, and $(y_1,y_2)=(500,1000)$ km. The choice of $\gamma^{-1}=3$ h corresponds to localized ITCZs while $\gamma^{-1}=6$ h is more likely in zonally elongated ITCZs. When γ^{-1} equals 12 or 24 h, transient activity in the Hadley circulation decreases substantially, as demonstrated in Figure 6. This can be explained by the ψ solutions in (51) approaching the balanced solutions in (53) as γ^{-1} increases. The spectral space solution (51) can be considered as the sum of two parts. The first part consists of the oscillatory terms $\cos(\nu_{mn}t)$ and $\sin(\nu_{mn}t)$; the second part contains the evanescent term with the $e^{-\gamma t}$ factor. Also, the term outside of the brackets happens to be the term in the steady state limit, Ψ_{mn}. For large times (i.e., $\gamma t \gg 1$), the second part is negligible and the oscillatory terms

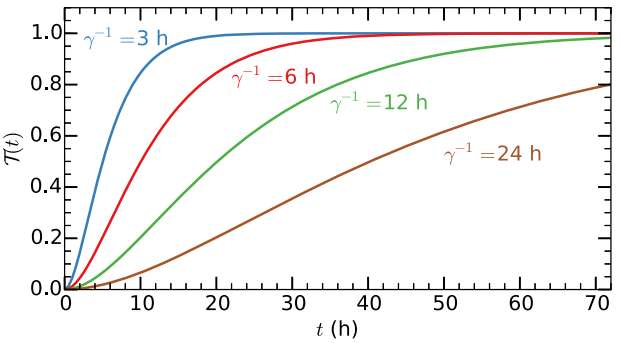

Figure 4. Plots of the switch-on function $\mathcal{T}(t)$ for the four choices $\gamma^{-1}=3,\ 6,\ 12,$ and 24 h. The "filtered solutions" are valid for the "slow switch-on" cases, i.e., for large values of γ^{-1}.

represent inertia-gravity waves that have propagated far from any confined region of forcing [*Salby and Garcia*, 1987; *Garcia et al.*, 1987].

The evanescent part of ψ changes very little after approximately 12 h in both Figures 5 and 6 while the oscillatory part of ψ continues to be active long after the forcing has been fully switched on, as demonstrated in Figure 5. When $\gamma^{-1}=3$ h, the southern and northern Hadley cells are almost symmetric in size and magnitude at $t=12$ h, but by $t=36$ h, the northern cell, which is typically thermally direct, has become thermally indirect. At $t=60$ h, the northern cell is both wider and stronger than the southern cell, and the opposite occurs at $t=84$ h. In addition to this transient activity there is an inherent asymmetry between the Hadley cells in a time averaged sense due to the anisotropy of the inertial stability [*Hack et al.*, 1989; *Gonzalez and Mora Rojas*, 2014]. This is even more clear in Figure 6, where the transient activity is not excited as effectively, implying that the zonal winds in the Hadley cells are essentially in geostrophic balance. Thus, we can refer to the Hadley circulation as a balanced Hadley circulation when the ITCZ diabatic heating is switched on slowly [*Gonzalez and Mora Rojas*, 2014]. When the diabatic heating in the ITCZ is switched on rapidly, there are both balanced and transient aspects to the Hadley circulation, where the transient activity is in the form of equatorially trapped inertia-gravity waves.

Since we have assumed a vertical structure composed of the single $m=1$ internal mode, the vertical structure of $\psi(y,z,t)$ is simply $e^{-z/2H}\mathfrak{Z}_1(z)$. Therefore, we analyze ψ where it maximizes in the vertical, at $z=5.7$ km. Figure 7 illustrates ψ as a function of time at $z=5.7$ km and at the southern edge of the ITCZ ($y=y_1$, southern Hadley cell) in the blue curves, northern edge of the ITCZ ($y=y_2$, northern Hadley cell) in the red curves, and the black curves represent the total mass flux, $\psi(y_2)-\psi(y_1)$. All curves are computed using the same parameter values as in Figure 5 and $\gamma^{-1}=3,6,12,24$ h in the four curves for each color. Note that the total mass flux, given by $\psi(y_2)-\psi(y_1)$, is strictly positive because $\psi(y_1)<0$ and $\psi(y_2)$ is either positive or near zero. The blue and red curves in Figure 7 show that both the southern and northern Hadley cells have similar oscillatory behavior but are out of phase, with the southern cell peaking in intensity about 20–30 h after the northern cell peaks in intensity. This lag occurs because the inertia-gravity waves that travel northward from the ITCZ reach their turning latitudes before the inertia-gravity waves traveling southward from the ITCZ. This behavior causes the northern cell strength to fluctuate significantly with time; it can be as strong as the southern cell and it can also disappear, as seen in Figures 5 and 7. The total mass flux in the ITCZ, shown in the black curves, also contains high frequency behavior due to the time lag between the two cells. Note that the time average asymmetry between the southern and northern cells is approximately 2 to 1 for all ITCZ switch on rates, similar to the balanced solutions shown in *Gonzalez and Mora Rojas* [2014].

Figure 8 illustrates the normalized power of ψ at the southern and northern edge of the ITCZ represented by the color shading and black line contours, respectively, as a function of frequency in h^{-1} and central ITCZ location $(y_1+y_2)/2$ for a 500 km wide ITCZ diabatic heating and for $\gamma^{-1}=6$ h. The power spectrum is computed by first removing the time mean of ψ, then performing a Hann window, and computing a discrete fast Fourier transform on the resulting time series. Note that the power in the shading and the black contours is normalized by the maximum power in the southern Hadley cell. The amplitude of the inertia-gravity waves in both Hadley cells maximize at an approximate timescale of 50 h and have their largest amplitude when the ITCZ is centered off of the equator. More specifically, the inertia-gravity wave amplitude peaks when $(y_1+y_2)/2\approx 1150$ km and 950 km in the southern and northern cell, respectively. These ITCZ locations nearly coincide with the ITCZ location where there is the maximum asymmetry between the southern and northern Hadley cells [*Hack et al.*, 1989; *Gonzalez and Mora Rojas*, 2014]. Also, the inertia-gravity waves in the southern cell are about twice as large in amplitude as those in the northern cell, similar to the time average

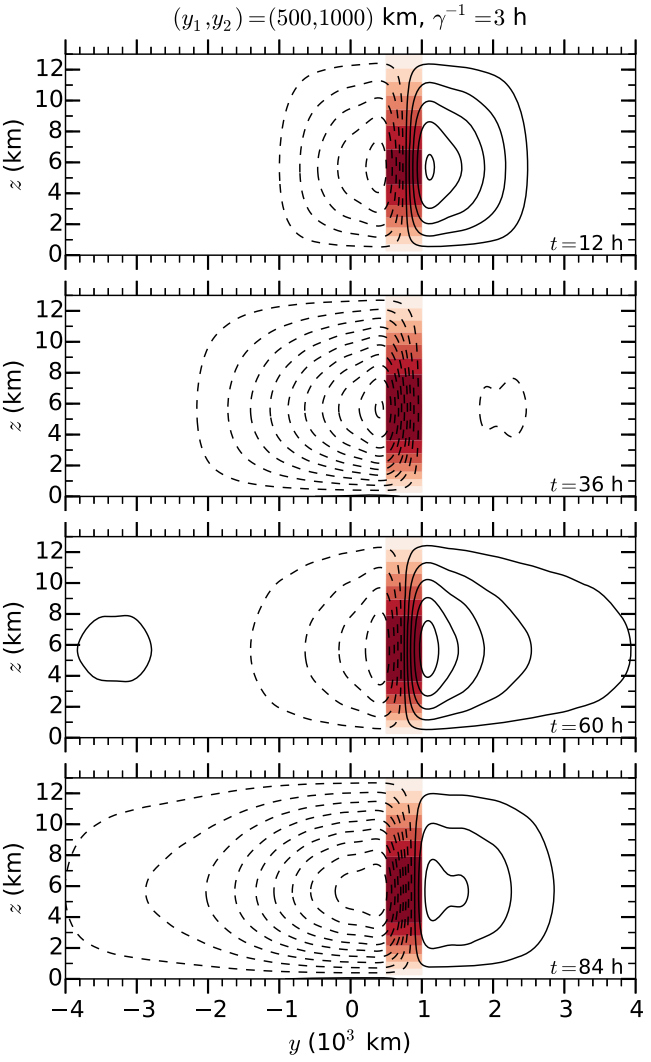

Figure 5. Contoured $\psi(y,z,t)$ and shaded $Q(y,z,t)e^{-z/H}/c_p$ fields for $(y_1, y_2) = (500, 1000)$ km, $m = 1$, and $\gamma^{-1} = 3$ h at $t = 12,\ 36,\ 60,\ 84$ h. The contour interval for $\psi(y,z,t)$ is 400 m^2 s^{-1}, the maximum (magnitude) of $\psi(y,z,t)$ is 4156 m^2 s^{-1}, and the zero line is omitted. The $Q(y,z,t)e^{-z/H}/c_p$ shade interval is 0.5 K d^{-1}, and the maximum (magnitude) of the diabatic heating is 3.496 K d^{-1}.

asymmetry between the two cells. Note that the northern cell also contains high frequency variability when $\gamma^{-1} = 3$ h (secondary peak near the 30 h timescale, not shown) because it is located farther away from the equator than the southern cell where the low n inertia-gravity waves have smaller amplitudes, as implied from the Hermite functions $\mathcal{H}_n^m(y)$ in Figure 2. When the ITCZ diabatic heating is switched on at the rate $\gamma^{-1} = 12$ h (not shown), the inertia-gravity wave activity decreases significantly, but variability is still largest near the 50 h timescale. It is not until $\gamma^{-1} = 24$ h that we see the 50 h variability associated with inertia-gravity waves becomes negligible.

Although we have focused on solutions for ψ thus far, we emphasize that the horizontal structure of v is the same as ψ. The $(\partial u/\partial t)$ field is also very similar to v, with an additional βy factor, as seen from (1). The w, $(\partial T/\partial t)$, and $(\partial \Phi/\partial t)$ fields have quite different horizontal structures than the ψ and v fields due to the meridional derivative of ψ in (9).

Figure 9 shows the "full solution" of w, the "evanescent part" of w, and the "oscillatory part" of w at $z = 7.6$ km (where it maximizes in the vertical) using the same parameters as Figure 8. Recall that the spectral space solution (51) can be considered as the sum of two parts, with the first part containing the oscillatory terms $\cos(\nu_{mn}t)$ and $\sin(\nu_{mn}t)$ and the second part containing the evanescent term with the $e^{-\gamma t}$ factor. Similar to the ψ field, the evanescent w solutions in the middle panel change very little after approximately 12 h while the inertia-gravity wave w solutions in the bottom panel continue to be active long after the forcing has been fully switched on. The oscillatory terms illustrate the equatorially trapped inertia-gravity wave activity in both Hadley cells, however, both the oscillatory and evanescent solutions are larger in the southern cell. Also, the irregular pulsation of the southern and northern cells occurs because the waves that emanate from the north edge of the ITCZ bounce off of their turning latitudes before those traveling from the south edge of the ITCZ bounce off of their turning latitudes. It is easier to trace individual paths, or rays, of the inertia-gravity wave packets in the w field than the ψ field, especially in the subsidence regions, as we discuss in more depth in section 7.

The "oscillatory" and "evanescent" parts of w are nonzero at $t = 0$, but their sum is zero, as seen in the "full solution" of w. This is similar to the classic f-plane geostrophic adjustment problem where the oscillatory and evanescent parts of the height field are initially nonzero, but their sum equals zero. In the classic geostrophic adjustment problem, the inertia-gravity waves satisfy f-plane dynamics rather than equatorial β-plane dynamics, so that the waves do not bounce back toward their source [*Gill*, 1982, section 7.3]. Another interesting feature of Figure 9 is that the top two panels reveal essentially time-independent spatial

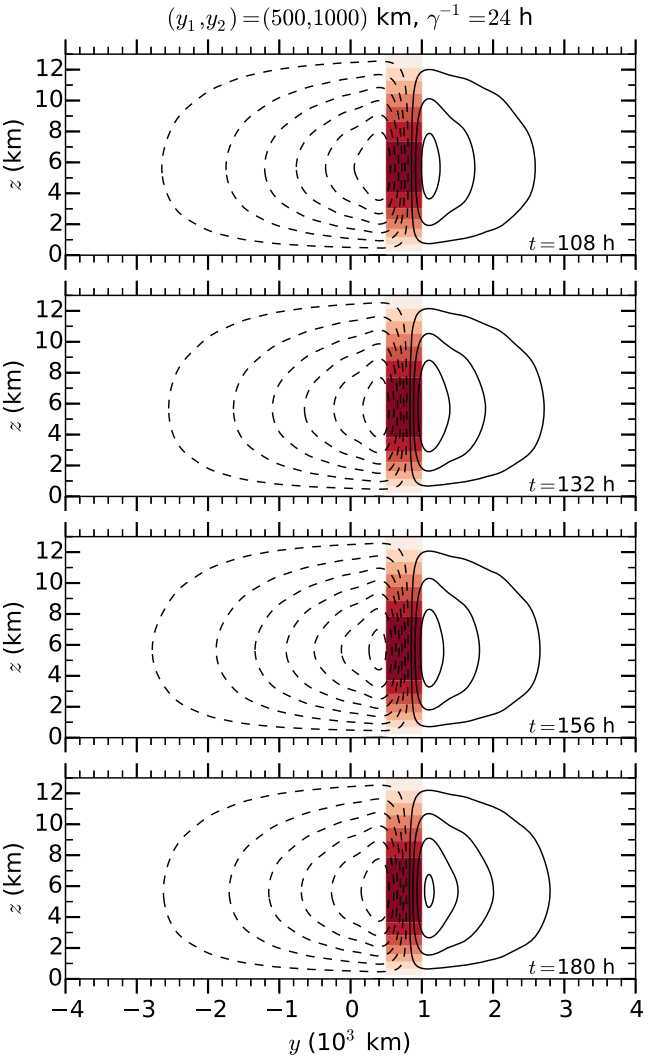

Figure 6. The same as Figure 5, but using $\gamma^{-1} = 24$ h and $t = 108, 132, 156, 180$ h. The maximum (magnitude) of $\psi(y, z, t)$ is 2818 m^2 s^{-1}.

oscillations in the evanescent part and in the full solution for *w*, especially in the subsiding regions (blue shading) on either side of the ITCZ. We do not regard these as physically significant, but rather as Gibbs phenomenon oscillations associated with the use of the Hermite representation in *y*, combined with the assumption (46) that the diabatic heating is discontinuous at the edges of the ITCZ. Interestingly, while the assumption of discontinuous diabatic heating leads to a very compact representation of the solution in terms of Green's functions [*Gonzalez and Mora Rojas*, 2014], it leads to this Gibbs phenomenon when the solution representation is in terms of the Hermite series in *y*.

Figure 10 shows the time evolution of the vertical log-pressure velocity *w* as a function of time at $z = 7.6$ km and at $y = 0$ km and $y = 1500$ km in the southern and northern Hadley cells in the blue and red curves, respectively, using the same parameter values as in Figure 7. These meridional locations can be thought of as representative of the subsidence regions in the southern and northern Hadley cells. The temporal evolution of the *w* field in the center of the ITCZ is not shown but essentially has the same behavior as the total mass flux in the ITCZ shown in Figure 7. There is a significant amount of transient activity in both subsidence regions in Figure 10. Subsidence in the southern cell is typically larger than the subsidence in the northern cell, as expected, but their vertical motion ratio is much smaller than their mass flux ratio. Both Hadley cells experience brief periods when their vertical motion transitions from subsidence to weak ascent, especially in the northern cell. Inertia-gravity wave activity is concentrated at a higher frequency than the 50 h timescale. Also, there seems to be significant transient activity at a secondary timescale.

Figure 11 illustrates the normalized power associated with *w* at $z = 7.6$ km and at $y = 0$ km (southern cell, colored shading) and $y = 1500$ km (northern cell, black contours) as a function of frequency in h^{-1} and central ITCZ location $(y_1 + y_2)/2$ for a 500 km wide ITCZ using the same parameters as Figure 8. Note that the power in the colored shading and the black contours is normalized by the maximum power in the southern Hadley cell. Transient convection in the ITCZ excites a range of frequencies in the *w* field subsidence regions, with the largest amplitude inertia-gravity waves peaking near 30 and 50 h periods. The 30 h timescale is most dominant when the ITCZ is close to the equator while the 50 h timescale is preferred when the ITCZ is far from the equator. More specifically, the southern Hadley cell is dominated by 30 h oscillations when the ITCZ is centered 0–7.5° off of the equator and 50 h oscillations when the ITCZ is centered 12.5–20° off of the equator. On the other hand, the northern Hadley cell is dominated by 30 h oscillations when the ITCZ is 0–2.5° off of the equator and 50 h oscillations when the ITCZ is 2.5–20° off of the equator. When the ITCZ is centered 7.5–12.5° off of the equator, the southern cell experiences oscillations at both 30 and

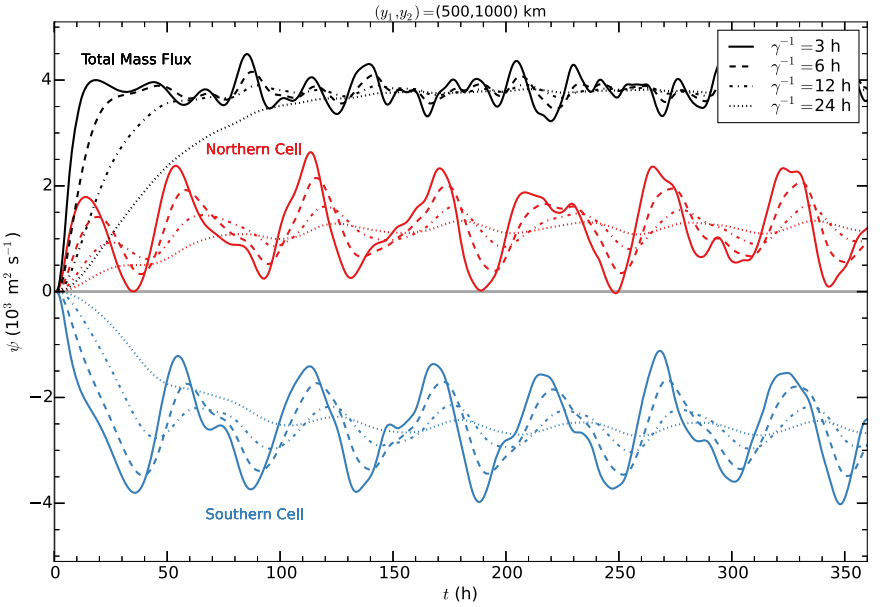

Figure 7. The time evolution of ψ as a function of time at $z = 5.7$ km and at the southern edge of the ITCZ ($y = y_1$, southern Hadley cell) in the blue curves, the northern edge of the ITCZ ($y = y_2$, northern Hadley cell) in the red curves, and the black curves represent the total mass flux ($\psi(y_2) - \psi(y_1)$) for the four ITCZ diabatic heating switch on rates $\gamma^{-1} = 3, 6, 12, 24$ h. All other parameters are the same as those in Figure 5.

50 h timescales. The vertical motion in the ITCZ, although not shown explicitly, is mainly dominated by 50 h oscillations when $\gamma^{-1} = 6$ h and by 30 h oscillations when $\gamma^{-1} = 3$ h.

6.2. Diabatic Heating of Other Modes

In this section, we examine the solutions for experiments where the vertical structure of the diabatic heating is composed of individual modes other than the $m = 1$ internal mode. It has been shown that diabatic heating in the ITCZ tends to contain contributions mainly from the $m = 0$ external mode and the $m = 1$ and 2 internal modes [*Fulton and Schubert*, 1985]. In particular, regions such as the Atlantic and eastern Pacific tend to have strong bimodal ($m = 1$, 2) variability in the vertical structure of diabatic heating [*Zhang and Hagos*, 2009].

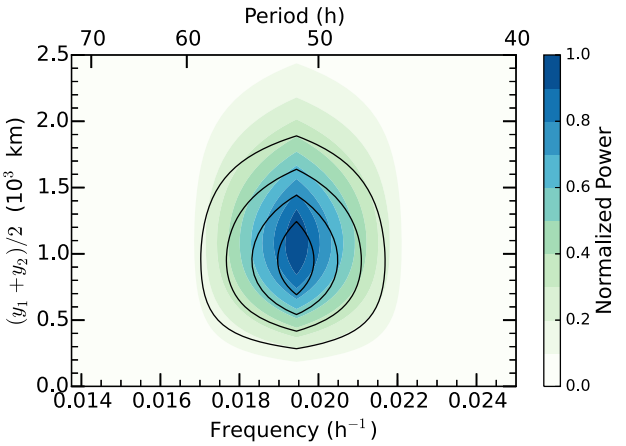

Figure 8. The normalized power associated with ψ at the southern and northern edge of the ITCZ represented by the color shading and black line contours, respectively, as a function of frequency in h^{-1} and central ITCZ location $(y_1+y_2)/2$ in km for the ITCZ diabatic heating switch on rate $\gamma^{-1} = 6$ h. All other parameters are the same as those in Figure 5. The shading and isoline contour interval is 0.1.

In Figure 12 we display ψ as a function of time at $z = 5.7$ km and at the southern and northern edge of the ITCZ in the blue and red curve, respectively, and the total mass flux, $\psi(y_2) - \psi(y_1)$, in the black curve using the same parameter values as in Figure 8, except for an ITCZ diabatic heating of the $m = 2$ internal mode. The ideas we have postulated thus far for the $m = 1$ diabatic forcing apply to the $m = 0$ (not shown) and $m = 2$ cases in that there is significant pulsating of the southern and northern Hadley cells due to equatorially trapped inertia-gravity waves. The pulsating for the $m = 2$ diabatic heating leads to slower-moving inertia-gravity wave packets than the $m = 1$ case, with the amplitude of inertia-gravity waves in ψ peaking at a period of approximately 70 h, while the pulsating for the $m = 0$

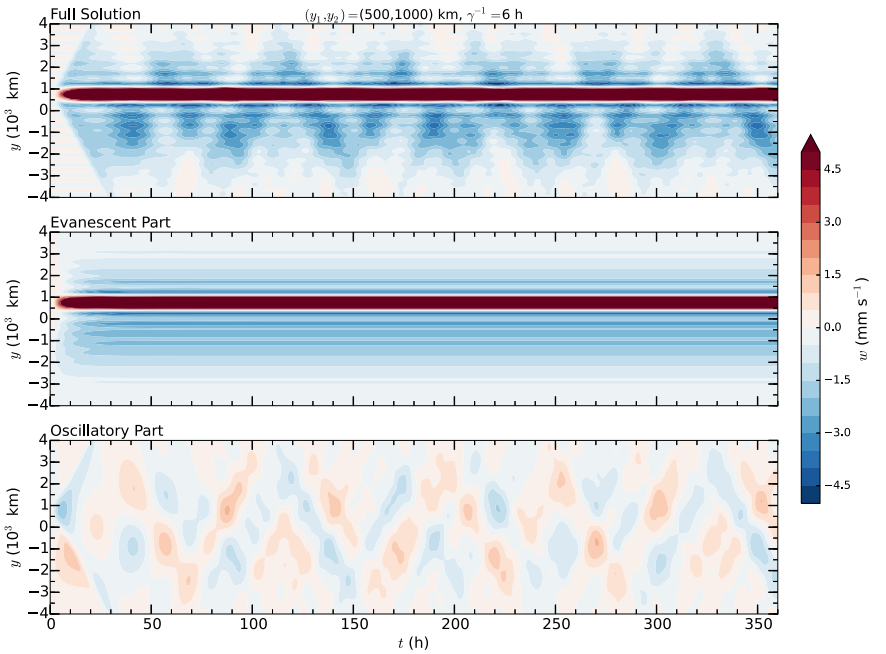

Figure 9. Solutions of $w(y, t)$ at $z = 7.6$ km: the "full solution" of w (top), the "evanescent part" of w (middle), and the "oscillatory part" of w (bottom) using the same parameters used in Figure 8.

diabatic heating leads to faster propagating inertia-gravity wave packets than the $m = 1$ case, corresponding to a period of approximately 20 h. These results can be explained by the internal gravity wave speed decreasing as a function of vertical wave number m even though the turning latitude decreases as m increases. This implies that the wave packets take longer to reach their critical latitudes as the vertical structure of diabatic heating becomes more complex (i.e., involving higher internal modes), leading to an excitation of lower frequencies of the entire tropical belt. In addition to the ψ field, these ideas apply to the transient behavior in the w field, e.g., the southern Hadley cell is dominated by 40 h oscillations when the ITCZ is centered 0–7.5° off of the equator and 70 h oscillations when the ITCZ is centered 12.5–20° off of the equator. On the other hand, the northern Hadley cell is dominated by 40 h oscillations when the ITCZ is 0–2.5° off of the equator and 70 h oscillations when the ITCZ is 2.5–20° off of the equator. A possible explanation for this behavior is that as the forcing involves higher vertical wave numbers, the asymmetry between the southern and northern cells increases, as discussed in *Gonzalez and Mora Rojas* [2014].

When diabatic heating in the ITCZ is convectively coupled to equatorial waves, the static stability is effectively smaller [*Wheeler and Kiladis*, 1999]. We can simulate this in our idealized model by decreasing the value of N, in which case the equatorially trapped wave packets travel slower. For an ITCZ diabatic heating of the $m = 0, 1, 2$ vertical modes in the region $(y_1, y_2) = (500, 1000)$ km with the new value of $N = 0.06$ s^{-1}, the peak transient activity in ψ occurs at approximately 70, 90, and 115 h timescales, respectively. Therefore, it is possible that inertia-gravity wave activity associated with the Hadley cells may occur at slightly different timescales in observations. We performed a preliminary spectral analysis of the meridional wind field during the months of July and August using the YOTC reanalysis at various locations in the eastern Pacific ITCZ and found there to be prominent peaks at 3–5 day timescales (not shown). This result is promising; however, we leave a more in-depth analysis to future work.

In concluding this section it is interesting to note that, as t becomes large, $\mathfrak{T}(t) \to 1$ and the evanescent part of the forced divergent circulation (v, w) comes into steady state. However, as can be seen from (1) and (5), the zonal flow and the temperature continue to evolve. In fact, as discussed by *Gonzalez and Mora Rojas* [2014], these fields evolve in such a way that the associated potential vorticity field develops local extrema in the ITCZ, leading to a zonal flow that satisfies the Charney-Stern necessary condition for combined barotropic-baroclinic instability [*Charney and Stern*, 1962]. Thus, one should not expect the evolving zonal flow to remain zonally symmetric for more than approximately a week [*Nieto Ferreira and Schubert*, 1997; *Wang and Magnusdottir*, 2005; *Magnusdottir and Wang*, 2008].

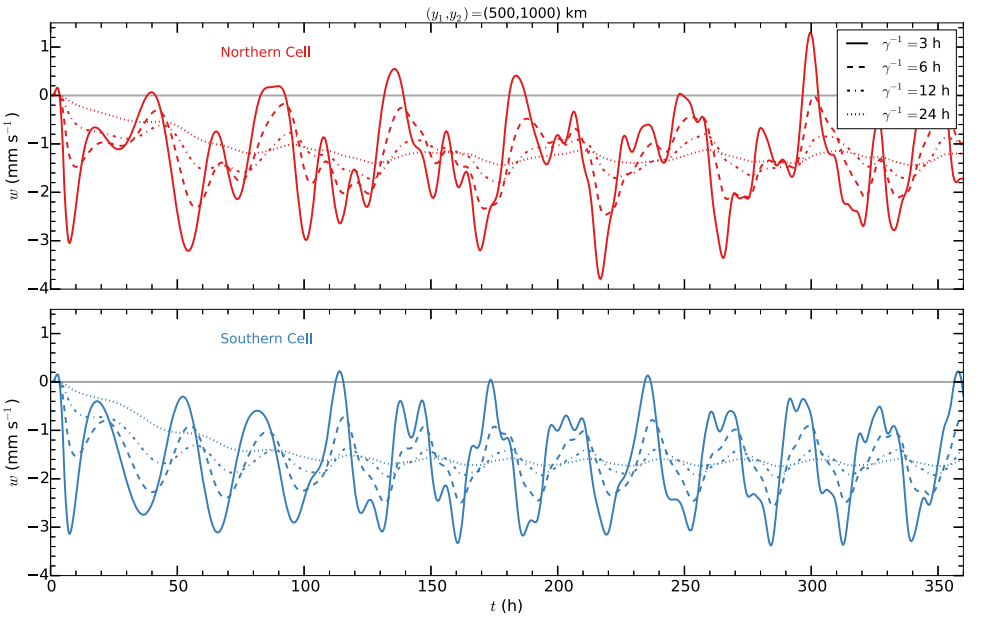

Figure 10. The time evolution of w at $z = 7.6$ km and in the two subsidence regions: the southern cell (at $y = 0$ km) in the blue curves and northern cell (at $y = 1500$ km) in the red curves. The four lines for each subsidence region represent the ITCZ diabatic heating switch on rates γ^{-1}=3, 6, 12, 24 h. All other parameters are the same as those in Figure 7.

7. Analysis of Inertia-Gravity Wave Packets

When the intensity of ITCZ convection fluctuates, inertia-gravity wave packets are emitted toward the north and south, as we have discussed in the previous section. The movement of these wave packets depends critically on the waveguide effect, i.e., the effect by which the variable Coriolis parameter traps the inertia-gravity wave energy in the equatorial region. We can understand this process via a variety of approaches, including the following three: (i) asymptotic results obtained from the exact solution (52); (ii) average conservation law approach [*Whitham*, 1965a]; (iii) variational approach [*Whitham*, 1965b, 1974, section 11.7]. Approaches (ii) and (iii) have the advantage that the exact solution of the problem is not required, i.e., the mathematical apparatus of Hermite transforms can be bypassed. Although the variational approach is the most general, approach (ii) is perhaps more easily understood and is presented in this section. For readers familiar with variational methods, approach (iii) is discussed in Appendix A.

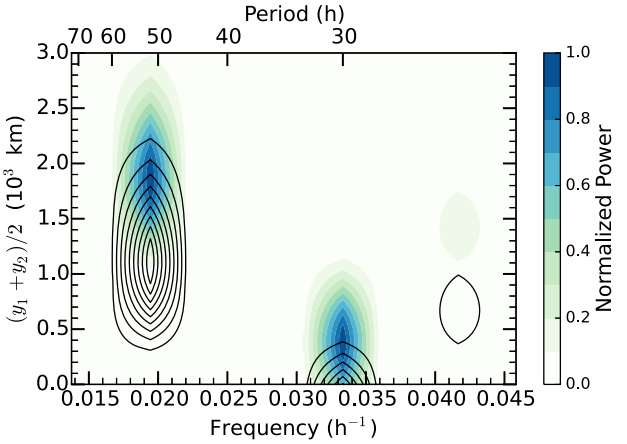

Figure 11. The normalized power associated with w in the southern and northern cell represented by the color shading and black line contours, respectively, as a function of frequency in h^{-1} and central ITCZ location $(y_1 + y_2)/2$ in km for the ITCZ diabatic heating switch on rate γ^{-1}=6 h. All other parameters are the same as those in Figure 8. The shading and isoline contour interval is 0.1.

The discussion of the average conservation law approach begins with the unforced version of the horizontal structure equation (28), written in the form

$$\psi_{tt} - c^2\psi_{yy} + \beta^2 y^2 \psi = 0, \qquad (56)$$

where, for simplicity, we have dropped the subscript m and the hat on ψ. The homogeneous equation (56) essentially describes the propagation of zonally symmetric inertia-gravity waves in the equatorial waveguide after they have been excited in the ITCZ, although this should be regarded as an approximation since a wave packet that is turned back through

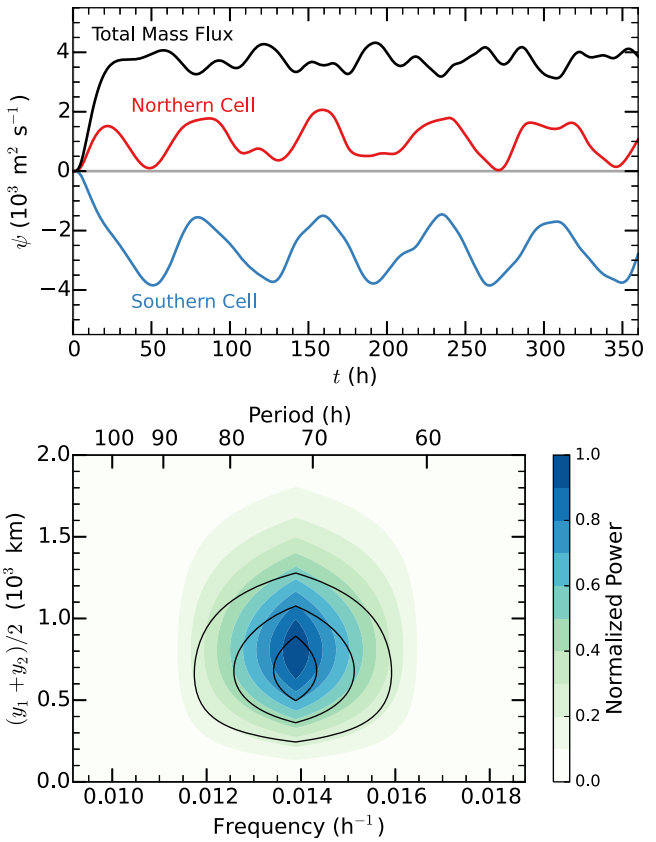

Figure 12. The top figure shows the time evolution of the stream function ψ at $z = 5.7$ km and at the southern and northern edge of the ITCZ in the blue and red curve, respectively, and the black curve represents the total mass flux, $\psi(y_2)-\psi(y_1)$, for an $m = 2$ ITCZ diabatic heating with the switch on rate $\gamma^{-1}=6$ h. The bottom figure illustrates the normalized power associated with ψ at $z = 5.7$ km and at the southern and northern edge of the ITCZ in the color shading and black line contours, respectively, as a function of frequency in h^{-1} and ITCZ central location $(y_1+y_2)/2$ in km. All other parameters are the same as in Figure 8.

the ITCZ could experience an additional forcing not accounted for in (56). If the factor β^2y^2 in (56) were replaced by a constant f^2, the resulting equation would be the classic *f*-plane geostrophic adjustment equation (i.e., the Klein-Gordon equation) studied by *Cahn* [1945]. Thus, the transient ITCZ adjustment problem is essentially a classic geostrophic adjustment problem, but with the interesting added effects produced by a variable Coriolis parameter.

Multiplying (56) by ψ_t, we obtain the energy conservation relation

$$\frac{\partial}{\partial t}\left[\frac{1}{2}\left(\psi_t^2+c^2\psi_y^2+\beta^2y^2\psi^2\right)\right] + \frac{\partial}{\partial y}\left(-c^2\psi_y\psi_t\right)=0. \tag{57}$$

Similarly, multiplying (56) by $-\psi_y$, we obtain the pseudomomentum conservation relation

$$\frac{\partial}{\partial t}\left(-\psi_y\psi_t\right) + \frac{\partial}{\partial y}\left[\frac{1}{2}\left(\psi_t^2+c^2\psi_y^2-\beta^2y^2\psi^2\right)\right]=-\beta^2y\psi^2. \tag{58}$$

The term on the right-hand side of (58) arises because the inertia-gravity waves propagate through a spatially nonuniform medium, with the nonuniformity due to the *y*-variation of the Coriolis parameter. An analogous term does not appear on the right-hand side of (57) because, although the medium is spatially nonuniform, it is not time-dependent.

We now search for solutions that have the form of a slowly varying wave train, i.e.,

$$\psi(y,t)=\text{Real}\left(A(y,t)e^{i\theta(y,t)}\right)=a(y,t)\cos\left(\theta(y,t)+\eta(y,t)\right), \tag{59}$$

where $\theta(y,t)$ is the phase, $a(y,t)=|A(y,t)|$ is the amplitude, and $\eta(y,t)=\arg A(y,t)$ is the phase shift. Differentiation of (59) yields

$$\begin{aligned}\psi_t&=-(\theta_t+\eta_t)a\sin(\theta+\eta)+a_t\cos(\theta+\eta),\\ \psi_y&=-(\theta_y+\eta_y)a\sin(\theta+\eta)+a_y\cos(\theta+\eta).\end{aligned} \tag{60}$$

Now assume that $a(y, t)$ and $\eta(y,t)$ are slowly varying so that the terms involving a_t, η_t, a_y, η_y can be neglected. Application of this approximation to (60) yields

$$\begin{aligned}\psi_t&=\omega a\sin(\theta+\eta),\\ \psi_y&=-\ell a\sin(\theta+\eta),\end{aligned} \tag{61}$$

where

$$\ell(y,t)=\frac{\partial\theta(y,t)}{\partial y} \quad \text{and} \quad \omega(y,t)=-\frac{\partial\theta(y,t)}{\partial t} \tag{62}$$

are the local meridional wave number and the local frequency, respectively. When these approximations are used in (56), we obtain the inertia-gravity wave dispersion relation

$$\omega^2=c^2\ell^2+\beta^2y^2. \tag{63}$$

In contrast to (42), equation (63) is a local dispersion relation relating the local frequency $\omega(y,t)$, the local wave number $\ell(y,t)$, and the latitude y. For our linear problem, the amplitude $a(y,t)$ does not appear in the local dispersion relation.

While the analytical solution (52) gives the complete structure of the ψ field, the present "slowly varying wave train analysis" gives a more macroscopic view of the ψ field. In this spirit, it is natural to apply a spatial running mean operator $\overline{(\ )}$ to the conservation equations (57) and (58). The spatial interval of this running mean operator is small compared to the scale of variation of $\ell(y,t)$, $\omega(y,t)$, and $a(y,t)$, but it includes one or more cycles of the phase θ. Application of this averaging operator to (57) and (58) results in

$$\frac{\partial}{\partial t}\left[\frac{1}{2}\left(\overline{\psi_t^2}+c^2\overline{\psi_y^2}+\beta^2y^2\overline{\psi^2}\right)\right]+\frac{\partial}{\partial y}\left(-c^2\overline{\psi_y\psi_t}\right)=0, \tag{64}$$

$$\frac{\partial}{\partial t}\left(-\overline{\psi_y\psi_t}\right)+\frac{\partial}{\partial y}\left[\frac{1}{2}\left(\overline{\psi_t^2}+c^2\overline{\psi_y^2}-\beta^2y^2\overline{\psi^2}\right)\right]=-\beta^2y\overline{\psi^2}. \tag{65}$$

Our goal is to use the average conservation equations (64) and (65), together with the local dispersion relation (63), to obtain governing equations for the slowly varying fields $\ell(y,t)$, $\omega(y,t)$, and $a(y,t)$. Since the mean values of $\sin^2(\theta+\eta)$ and $\cos^2(\theta+\eta)$ over one oscillation are both equal to 1/2, we obtain from (61) the following relations for the mean values appearing in (64) and (65)

$$\begin{aligned}&\overline{\psi_t^2}=\frac{1}{2}\omega^2a^2, \qquad \overline{\psi_y^2}=\frac{1}{2}\ell^2a^2,\\ &\overline{\psi^2}=\frac{1}{2}a^2, \qquad -\overline{\psi_y\psi_t}=\frac{1}{2}\ell\omega a^2.\end{aligned} \tag{66}$$

Using (66) in (64) and (65) we obtain the average conservation equations in the forms

$$\frac{\partial}{\partial t}\left(\omega^2a^2\right)+\frac{\partial}{\partial y}\left(c^2\ell\omega a^2\right)=0, \tag{67}$$

$$\frac{\partial}{\partial t}\left(\ell\omega a^2\right)+\frac{\partial}{\partial y}\left(c^2\ell^2a^2\right)=-\beta^2ya^2, \tag{68}$$

where we have used the dispersion relation (63) in both (67) and (68). The energy conservation equation (67) can also be written as

$$\frac{\partial\mathcal{E}}{\partial t}+\frac{\partial(c_g\mathcal{E})}{\partial y}=0, \tag{69}$$

where the energy density $\mathcal{E}(y,t)$ and the group velocity $c_g(y,t)$ are given by

$$\mathcal{E}=\frac{1}{2}\omega^2a^2 \quad \text{and} \quad c_g=\frac{c^2\ell}{\omega}. \tag{70}$$

Using (69) and the dispersion relation (63), it can be shown that the conservation equation (68) leads to

$$\frac{\partial\omega}{\partial t}+c_g\frac{\partial\omega}{\partial y}=0. \tag{71}$$

According to (69), the total energy in the area between two group lines remains fixed.

Since the characteristic forms of (69) and (71) are

$$\left.\begin{aligned}\frac{d\mathcal{E}}{dt}&=-\frac{\partial c_g}{\partial y}\mathcal{E}\\ \frac{d\omega}{dt}&=0\end{aligned}\right\}\quad\text{on}\quad\frac{dy}{dt}=c_g, \tag{72}$$

the frequency ω is invariant along a group line, while the energy density $\mathcal{E}$ decays or grows along a group line due to the divergence or convergence of the group lines. Another form of (72) is

$$\left.\begin{aligned}\frac{da}{dt}&=-\frac{1}{2}\frac{\partial c_g}{\partial y}a\\ \frac{d\omega}{dt}&=0\end{aligned}\right\}\quad\text{on}\quad\frac{dy}{dt}=\pm\frac{c^2(\omega^2-\beta^2y^2)^{1/2}}{\omega}. \tag{73}$$

Note that the equations for ω and y are decoupled from the equation for a.

Now we would like to plot ray trajectories for choices of ω. Using the local dispersion relation (63), we can write $(dy/dt)=c_g$ in the form

$$\frac{dy}{(\omega^2-\beta^2y^2)^{1/2}}=\pm\frac{c\,dt}{\omega}. \tag{74}$$

Integration of (74) yields the solution

$$y(t;\omega,y_0,c)=\left(\frac{\omega}{\beta}\right)\sin\left\{\sin^{-1}\left(\frac{\beta y_0}{\omega}\right)\pm\frac{\beta ct}{\omega}\right\}. \tag{75}$$

For given values of ω, y_0, and c, (75) describes two ray trajectories, one starting at y_0 and initially moving northward, and the other also starting at y_0 but initially moving southward. Plots of $y(t;\omega,y_0,c)$ are shown in Figure 13 for $c=47.45$ m s^{-1} (the $m=1$ vertical mode), $y_0=500$ km and $y_0=1000$ km, and the two frequencies $\omega=(3\,\text{h})^{-1}$ and $\omega=(12\,\text{h})^{-1}$. The blue and red curves in Figure 13 represent the ray trajectories that initially move southward and northward, respectively. These frequencies are chosen to correspond with the switch-on rates of γ^{-1} that we analyzed previously. Note that low frequencies, such as $\omega=(12\,\text{h})^{-1}$ and $\omega=(24\,\text{h})^{-1}$, do not yield ray trajectories for y_0 poleward of a particular meridional location (e.g., $y_0=$ 1000 km for $\omega=(12\,\text{h})^{-1}$, in Figure 13). This is because these trajectories are beyond their turning latitudes.

The ray trajectories shown in Figure 13 turn back toward the equator at their turning latitudes, $\pm$4000 and $\pm$900 km. Recall that we introduced turning latitudes in the previous section, but because we have abandoned the idea of meridional modes n, the turning latitudes seen in Figure 13 do not correspond to any particular meridional mode n. The solutions presented in the last section are summed over all meridional modes, therefore they contain information about all of the meridional modes, but with varying amplitudes $\psi_{mn}(y,t)$. When the wave packets reach their turning latitude, their local meridional wave number crosses $\ell=0$, and the analysis breaks down [*Wunsch and Gill*, 1976]. Plots of $y(t)$ and $\ell(t)$ for $m=0$, 2 using the same two meridional wave numbers ℓ as in Figure 13 are similar to the plots shown in Figure 13, with particles traveling faster for $m=0$ and slower for $m=2$ along their ray trajectories due to c increasing when $m=0$ and c decreasing when $m=2$ (not shown), as we would expect from the results shown in section 6. Also, the ray trajectories spread out over time, in general agreement with (72).

8. Concluding Remarks

To understand the transient dynamics of meridional overturning circulations, a zonally symmetric model on the equatorial β-plane has been formulated and its associated meridional circulation equation has been derived. This meridional circulation equation is a partial differential equation in (y, z, t). It contains two types of forcing: (1) horizontal variation of the interior diabatic heating; (2) Ekman pumping at the top of the boundary layer. Since the problem is linear, the meridional circulations attributable to these two forcing effects can be treated separately, and then the resulting flows can simply be added together to obtain the

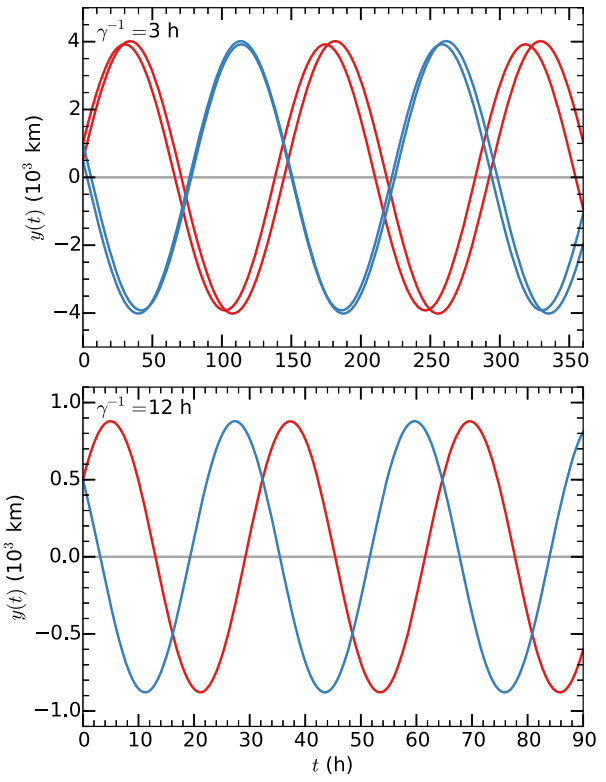

Figure 13. Plots of (75) for $m = 1$ and the switch-on rates $\gamma^{-1}=3$ h and $\gamma^{-1}=12$ h. The blue and red curves represent the ray trajectories that initially move southward and northward, respectively. Note how the rays turn at particular latitudes, approximately ± 4000 km for $\gamma^{-1}=3$ h and approximately ± 900 km for $\gamma^{-1}=12$ h.

total response. In this study we focus on the free tropospheric response to off-equatorial transient diabatic heating in the ITCZ.

The meridional circulation equation has been solved analytically by first performing a vertical transform that converts the partial differential equation in (y, z, t) into a system of partial differential equations in (y, t) for the meridional structures of all the vertical modes m. These partial differential equations have been solved via both the Green's function approach (evanescent basis functions) in *Gonzalez and Mora Rojas* [2014] and the Hermite transform approach (oscillatory basis functions) in this study. These two approaches yield two different mathematical representations of the same physical solution; for understanding the transient behavior of the Hadley cells, it is advantageous to solve the equations using Hermite functions. The solutions suggest that the Hadley cells contain inertia-gravity wave packets that emanate from the ITCZ and bounce off a spectrum of turning latitudes when convection in the ITCZ is temporally evolving. These equatorially trapped wave packets cause the mass flux associated with the Hadley cells to pulsate with periods of about 1, 2, and 3 days for the $m = 0$, 1, 2 vertical modes while the vertical motion in the ITCZ and subsidence regions are slightly more complicated and depend on ITCZ location, e.g., transient activity in the southern Hadley cell peaks at timescales of approximately 30 h and 2 days for ITCZs 0–7.5 and 12.5–20° off of the equator, respectively, for ITCZ diabatic heating of the $m = 1$ vertical mode. When the $m = 1$ ITCZ is centered 7.5–12.5° off of the equator, the southern cell experiences oscillations at both 30 and 50 h timescales. When the forcing is switched on slowly (e.g., about 80% switched on after 3 days), the transient behavior decreases significantly and the solutions are similar to the balanced results shown in *Gonzalez and Mora Rojas* [2014].

There have been a number of studies that have explored inertia-gravity waves forced by tropical convection, but not in the context of the ITCZ and the Hadley circulation. In regions such as the Pacific Ocean, the dynamics are nearly zonally symmetric; therefore, the analytical solutions derived can provide realistic insight into the dynamics. In other regions, such as the Indian Ocean, the assumption of zonal symmetry is not often met; therefore, the inertia-gravity waves emanating from tropical convection likely behave differently. We expect that these inertia-gravity waves travel in both the zonal and meridional directions, possibly bearing resemblance to the two-day inertia-gravity waves discussed in *Takayabu* [1994] and *Haertel and Kiladis* [2004]. In closing, we emphasize that the tropical atmosphere may contain a considerable amount of inertia-gravity wave activity, but its contribution to the large-scale flow may be difficult to discern in observational analyses. Therefore, this theoretical work should serve as motivation for future observational work on inertia-gravity waves in the tropics.

Appendix A: Variational Approach

As a complement to the analysis in section 7, we now discuss the variational approach to understanding the inertia-gravity wave aspects of the transient solutions. The argument again begins with (56), which is

the unforced version of the horizontal structure equation (28). We first note that (56) has the equivalent variational formulation

$$\delta \int\int L(\psi_t, \psi_y, \psi, y)\, dt\, dy = 0, \tag{A1}$$

where the Lagrangian is given by

$$L(\psi_t, \psi_y, \psi, y) = \frac{1}{2}\psi_t^2 - \frac{1}{2}c^2\psi_y^2 - \frac{1}{2}\beta^2 y^2 \psi^2. \tag{A2}$$

To confirm the equivalence of the variational formulation (A1) and (A2) with the partial differential equation (56), note that

$$\begin{aligned} 0 &= \delta \int\int L(\psi_t, \psi_y, \psi)\, dt\, dy \\ &= \int\int \left[\frac{\partial L}{\partial \psi_t}\delta\left(\frac{\partial \psi}{\partial t}\right) + \frac{\partial L}{\partial \psi_y}\delta\left(\frac{\partial \psi}{\partial y}\right) + \frac{\partial L}{\partial \psi}\delta\psi \right] dt\, dy \\ &= \int\int \left[-\frac{\partial}{\partial t}\left(\frac{\partial L}{\partial \psi_t}\right) - \frac{\partial}{\partial y}\left(\frac{\partial L}{\partial \psi_y}\right) + \frac{\partial L}{\partial \psi} \right] \delta\psi\, dt\, dy, \end{aligned} \tag{A3}$$

where the last line has been obtained through integration by parts in both t and y. It follows from (A3) that

$$\frac{\partial}{\partial t}\left(\frac{\partial L}{\partial \psi_t}\right) + \frac{\partial}{\partial y}\left(\frac{\partial L}{\partial \psi_y}\right) - \frac{\partial L}{\partial \psi} = 0. \tag{A4}$$

Differentiating (A2) we obtain

$$\frac{\partial L}{\partial \psi_t} = \psi_t, \quad \frac{\partial L}{\partial \psi_y} = -c^2\psi_y, \quad \frac{\partial L}{\partial \psi} = -\beta^2 y^2 \psi, \tag{A5}$$

which, when substituted into (A4), leads directly to (56).

In order to study slowly varying wave trains of the form $\psi \sim a\cos(\theta + \eta)$, *Whitham* [1965b, 1974, section 11.7] introduced the concept of an "average variational principle," which is analogous to (A1) and takes the form

$$\delta \int\int \mathfrak{L}(-\theta_t, \theta_y, a, y)\, dt\, dy = 0, \tag{A6}$$

where the local frequency and wave number are given by $\omega = -\theta_t$ and $\ell = \theta_y$, and where the average Lagrangian is given by

$$\mathfrak{L}(\omega, \ell, a, y) = \frac{1}{4}\left(\omega^2 - c^2\ell^2 - \beta^2 y^2\right)a^2. \tag{A7}$$

The average variational principle (A6) can then be written as

$$\begin{aligned} 0 &= \delta \int\int \mathfrak{L}(-\theta_t, \theta_y, a, y)\, dt\, dy \\ &= \int\int \left[\frac{\partial \mathfrak{L}}{\partial \theta_t}\delta\left(\frac{\partial \theta}{\partial t}\right) + \frac{\partial \mathfrak{L}}{\partial \theta_y}\delta\left(\frac{\partial \theta}{\partial y}\right) + \frac{\partial \mathfrak{L}}{\partial a}\delta a \right] dt\, dy \\ &= \int\int \left\{ \left[-\frac{\partial}{\partial t}\left(\frac{\partial \mathfrak{L}}{\partial \theta_t}\right) - \frac{\partial}{\partial y}\left(\frac{\partial \mathfrak{L}}{\partial \theta_y}\right) \right] \delta\theta + \frac{\partial \mathfrak{L}}{\partial a}\delta a \right\} dt\, dy, \end{aligned} \tag{A8}$$

where the last line has again been obtained through integration by parts in both t and y. Independent variations δa and $\delta\theta$ respectively yield

$$\frac{\partial \mathcal{L}}{\partial a}=0, \tag{A9}$$

$$\frac{\partial}{\partial t}\left(\frac{\partial \mathcal{L}}{\partial \omega}\right)-\frac{\partial}{\partial y}\left(\frac{\partial \mathcal{L}}{\partial \ell}\right)=0. \tag{A10}$$

Differentiating (A7) we obtain

$$\frac{\partial \mathcal{L}}{\partial \omega}=\frac{1}{2}\omega a^2, \quad \frac{\partial \mathcal{L}}{\partial \ell}=-\frac{1}{2}c^2\ell a^2, \quad \frac{\partial \mathcal{L}}{\partial a}=\frac{1}{2}(\omega^2-c^2\ell^2-\beta^2y^2)a, \tag{A11}$$

which, when substituted into (A9) and (A10), lead directly to the local dispersion relation

$$\omega^2=c^2\ell^2+\beta^2y^2, \tag{A12}$$

and to the wave action equation

$$\frac{\partial}{\partial t}\left(\frac{\mathcal{E}}{\omega}\right)+\frac{\partial}{\partial y}\left(c_g\frac{\mathcal{E}}{\omega}\right)=0, \tag{A13}$$

where $\mathcal{E}=\frac{1}{2}\omega^2a^2$ is the energy density, $\mathcal{E}/\omega$ is the wave action, and the group velocity is given by $c_g=c^2\ell/\omega$. The dispersion relation links the local meridional wave number $\ell(y,t)$ and the local frequency $\omega(y,t)$ of the nonuniform wave train propagating in a medium with variable Coriolis parameter βy.

From the relations $\omega=-\theta_t$ and $\ell=\theta_y$, it follows that $\ell_t+\omega_y=0$. Then, since the local dispersion relation yields $\omega_t=c_g\ell_t$, we conclude that

$$\frac{\partial \omega}{\partial t}+c_g\frac{\partial \omega}{\partial y}=0. \tag{A14}$$

Note that (A14) is identical to (71) and that (A13) and (A14) can be combined to obtain (69). In other words, the average conservation law approach of section 7 yields the same results as the variational approach. However, the variational approach gives a more direct route to the wave action principle (A13).

In section 7 and this appendix we have limited our discussion to the zonally symmetric case. Interesting discussions of ray theory for the zonally asymmetric case can be found in *Blandford* [1966] and *Ripa* [1994].

Acknowledgments

We thank two anonymous reviewers and Dave Nolan for their constructive comments that helped improve this paper significantly. We would also like to thank Thomas Birner, Eric Maloney, Donald Estep, Mark DeMaria, Scott Fulton, David Randall, Chris Slocum, James Ruppert, and Sue van den Heever for insightful discussions regarding this work. Research support for the authors has been provided by the National Science Foundation under grants AGS-1250966 and AGS-1546610, and under the Science and Technology Center for Multi-Scale Modeling of Atmospheric Processes, managed by Colorado State University through cooperative agreement ATM-0425247. The calculations were made on a Linux workstation provided through a gift from the Hewlett-Packard Corporation. The model and all data produced from the model simulations are available from the authors upon request (alex.o.gonzalez@jpl.nasa.gov).

References

Blandford, R. (1966), Mixed gravity-Rossby waves in the ocean, *Deep Sea Res. Oceanogr. Abstr.*, *13*, 941–961.

Cahn, A. (1945), An investigation of the free oscillations of a simple current system, *J. Meteorol.*, *2*, 113–119, doi:10.1175/1520-0469(1945)002<0113:AIOTFO>2.0.CO;2.

Cau, P., J. Methven, and B. J. Hoskins (2007), Origins of dry air in the tropics and subtropics, *J. Clim.*, *20*, 2745–2759.

Chao, W. C. (1987), On the origin of the tropical intraseasonal oscillation, *J. Atmos. Sci.*, *44*, 1940–1949.

Charney, J. G. (1955), The use of the primitive equations of motion in numerical forecasting, *Tellus*, *7*, 22–26.

Charney, J. G., and M. E. Stern (1962), On the stability of internal baroclinic jets in a rotating atmosphere, *J. Atmos. Sci.*, *19*, 159–172.

Daley, R. (1981), Normal mode initialization, *Rev. Geophys.*, *19*(3), 450–468, doi:10.1029/RG019i003p00450.

Evan, S., and M. J. Alexander (2008), Intermediate-scale tropical inertia gravity waves observed during the TWP-ICE campaign, *J. Geophys. Res.*, *113*, D14104, doi:10.1029/2007JD009289.

Evan, S., M. J. Alexander, and J. Dudhia (2012), Model study of intermediate-scale tropical inertia-gravity waves and comparison to TWP-ICE campaign observations, *J. Atmos. Sci.*, *69*(2), 591–610, doi:10.1175/JAS-D-11-051.1.

Fulton, S. R., and W. H. Schubert (1985), Vertical normal mode transforms: Theory and application, *Mon. Weather Rev.*, *113*, 647–658.

Galewsky, J., A. Sobel, and I. Held (2005), Diagnosis of subtropical humidity dynamics using tracers of last saturation, *J. Atmos. Sci.*, *62*, 3353–3367.

Garcia, R. R., and M. L. Salby (1987), Transient response to localized episodic heating in the tropics: Part II: Far-field behavior, *J. Atmos. Sci.*, *44*, 499–532.

Gill, A. E. (1980), Some simple solutions for heat-induced tropical circulation, *Q. J. R. Meteorol. Soc.*, *106*, 447–462.

Gill, A. E. (1982), *Atmosphere-Ocean Dynamics*, Academic, San Diego, Calif.

Gonzalez, A. O., and G. Mora Rojas (2014), Balanced dynamics of deep and shallow Hadley circulations in the tropics, *J. Adv. Model. Earth Syst.*, *6*, 777–804, doi:10.1002/2013MS000278.

Hack, J. J., and W. H. Schubert (1990), Some dynamical properties of idealized thermally-forced meridional circulations in the tropics, *Meteorol. Atmos. Phys.*, *44*, 101–117.

Hack, J. J., W. H. Schubert, D. E. Stevens, and H.-C. Kuo (1989), Response of the Hadley circulation to convective forcing in the ITCZ, *J. Atmos. Sci.*, *46*, 2957–2973.

Haertel, P. T., and G. N. Kiladis (2004), Dynamics of 2-day equatorial waves, *J. Atmos. Sci.*, *61*, 2707–2721.

Karoly, D. J., G. L. Roff, and M. J. Reeder (1996), Gravity wave activity associated with tropical convection detected in TOGA COARE Sounding data, *Geophys. Res. Lett.*, *23*(3), 261–264, doi:10.1029/96GL00023.

Lindzen, R. S., and A. V. Hou (1988), Hadley circulations for zonally averaged heating centered off the equator, *J. Atmos. Sci.*, *45*(17), 2416–2427, doi:10.1175/1520-0469(1988)045<2416:HCFZAH>2.0.CO;2.
Magnusdottir, G., and C.-C. Wang (2008), Intertropical convergence zones during the active season in daily data, *J. Atmos. Sci.*, *65*, 2425–2436.
Nieto Ferreira, R., and W. H. Schubert (1997), Barotropic aspects of ITCZ breakdown, *J. Atmos. Sci.*, *54*, 251–285.
Oort, A. H., and E. M. Rasmusson (1970), On the annual variation of the monthly mean meridional circulation, *Mon. Weather Rev.*, *98*(6), 423–442, doi:10.1175/1520-0493(1970)098<0423:OTAVOT>2.3.CO;2.
Pierrehumbert, R. T. (1998), Lateral mixing as a source of subtropical water vapor, *Geophys. Res. Lett.*, *25*(2), 151–154.
Pierrehumbert, R. T., and R. Roca (1998), Evidence for control of Atlantic subtropical humidity by large scale advection, *Geophys. Res. Lett.*, *25*(24), 4537–4540.
Ripa, P. (1994), Horizontal wave propagation in the equatorial waveguide, *J. Fluid Mech.*, *271*, 267–284.
Salathé, E., and D. Hartmann (1997), A trajectory analysis of tropical upper-tropospheric moisture and convection, *J. Clim.*, *10*, 2533–2547.
Salby, M. L., and R. R. Garcia (1987), Transient response to localized episodic heating in the tropics: Part I: Excitation and short-time near-field behavior, *J. Atmos. Sci.*, *44*, 458–498.
Schreck, C. J., L. Shi, J. P. Kossin, and J. J. Bates (2013), Identifying the MJO, equatorial waves, and their impacts using 32 years of HIRS upper-tropospheric water vapor, *J. Clim.*, *26*, 1418–1431.
Schubert, W. H., P. E. Ciesielski, D. E. Stevens, and H.-C. Kuo (1991), Potential vorticity modeling of the ITCZ and the Hadley circulation, *J. Atmos. Sci.*, *48*, 1493–1509.
Schubert, W. H., L. G. Silvers, M. T. Masarik, and A. O. Gonzalez (2009), A filtered model of tropical wave motions, *J. Adv. Model. Earth Syst.*, *1*, 1–13, doi:10.3894/JAMES.2009.1.3.
Sherwood, S. C., E. R. Kursinski, and W. G. Read (2006), A distribution law for free-tropospheric relative humidity, *J. Clim.*, *19*, 6267–6277.
Soden, B. J., and R. Fu (1995), A satellite analysis of deep convection, upper-tropospheric humidity, and greenhouse effect, *J. Clim.*, *8*, 2333–2351.
Sun, D.-Z., and R. Lindzen (1993), Distribution of tropical tropospheric water vapor, *J. Atmos. Sci.*, *50*, 1643–1660.
Takayabu, Y. N. (1994), Large-scale cloud disturbances associated with equatorial waves: Part II: Westward-propagating inertia-gravity waves, *J. Meteorol. Soc. Jpn.*, *72*, 451–465.
Tsuda, T., Y. Murayama, H. Wiryosumarto, S. W. B. Harijono, and S. Kato (1994), Radiosonde observations of equatorial atmosphere dynamics over Indonesia: 2. Characteristics of gravity waves, *J. Geophys. Res.*, *99*(D5), 10,507–10,516, doi:10.1029/94JD00354.
Wang, C.-C., and G. Magnusdottir (2005), ITCZ breakdown in three-dimensional flows, *J. Atmos. Sci.*, *62*, 1497–1512.
Wheeler, M., and G. N. Kiladis (1999), Convectively coupled equatorial waves: Analysis of clouds and temperature in the wavenumber frequency domain, *J. Atmos. Sci.*, *56*, 374–399.
Whitham, G. B. (1965a), Non-linear dispersive waves, in *Proceedings of the Royal Society of London Series A—Mathematical and Physical Sciences*, vol. *283*, pp. 238–261, R. Soc. of London, London, doi:10.1098/rspa.1965.0019.
Whitham, G. B. (1965b), A general approach to linear and non-linear dispersive waves using a Lagrangian, *J. Fluid Mech.*, *22*, 273–283, doi:10.1017/S0022112065000745.
Whitham, G. B. (1974), *Linear and Nonlinear Waves*, John Wiley, New York.
Wunsch, C., and A. E. Gill (1976), Observations of equatorially trapped waves in Pacific sea level variations, *Deep Sea Res. Oceanogr. Abstr.*, *23*, 371–390.
Zhang, C., and S. M. Hagos (2009), Bi-modal structure and variability of large-scale diabatic heating in the tropics, *J. Atmos. Sci.*, *66*, 3621–3640.